Seismic precast concrete shear walls with short-grouted ductile reinforcing bar connections

Baha'a Al-Khateeb, Christopher Garcia, Mark P. Manning, Jon Mohle, and Yahya C. Kurama

- This paper studies the use of short-grouted corrugated steel duct connectors for energy-dissipation reinforcing bars in seismic precast concrete construction.
- The research focuses on the performance of short-grouted corrugated steel duct connectors in three precast concrete shear wall specimens tested under reversed-cyclic lateral loading.
- The performance of the specimens is evaluated against seismic acceptance criteria for special precast concrete shear walls and design recommendations are made based on the performance differences among the specimens.

Grouted mechanical splices for reinforcing bars are allowed in seismic precast concrete shear walls by the American Concrete Institute's *Requirements for Design of a Special Unbonded Post-Tensioned Precast Shear Wall Satisfying ACI 550.6* (ACI 550.7-19).[1] Grouted bar splices are preferred in precast concrete construction because using the full development length required by the *Building Code Requirements for Structural Concrete (ACI 318-19) and Commentary (ACI 318R-19)*[2] is typically less practical for the handling, transportation, and erection of precast concrete components. However, previous experimental research[3–5] has demonstrated that grouted mechanical splices that satisfy the Type II splice requirements of ACI 318-19 are not adequate to develop ASTM A706[6] Grade 60 (414 MPa) energy-dissipation reinforcing bars (that is, reinforcing bars designed to yield and dissipate energy during a seismic event) crossing the base joint of precast concrete walls tested according to ACI 550.6-19, *Acceptance Criteria for Special Unbonded Post-Tensioned Precast Structural Walls Based on Validation Testing and Commentary*.[7] Specifically, premature pullout failure of energy-dissipation bars grouted inside Type II splices in a hybrid precast concrete shear wall[4] showed that these bars were subjected to higher strains with larger number of cycles than the strains and number of cycles required to validate Type II splices by the ICC Evaluation Services' *Acceptance Criteria for Mechanical Connector Systems for Steel Reinforcing Bars* (AC133).[8]

To address the need for ductile reinforcing bar connectors in special precast concrete shear walls satisfying the perfor-

mance requirements of ACI 550.6-19, Aragon et al.[9–11] tested a series of 20 jointed precast concrete specimens under cyclic uniaxial loading. Each specimen included a single ASTM A706 Grade 60 (414 MPa) reinforcing bar that crossed the precast concrete joint and was developed and terminated (without a splice) inside a nonproprietary, short-grouted ductile reinforcing bar connector. Each reinforcing bar connector used a thin 26 gauge (0.018 in. [0.45 mm] thick) steel duct (sleeve, conduit) with and without corrugations, and with and without a taper along the length of the duct. In this type of connection, the bar forces are transferred into precast concrete components through the design of vertical, transverse, and longitudinal tie reinforcing bars around the connectors. Connectors were tested using three different commercially available grout products, with the tests including adverse conditions simulated by intentionally using excess water in the grout mixture and by misaligning the bars inside the ducts.

Reinforcing bar connections using grouted metallic ducts are discussed in the *PCI Design Handbook* (MNL 120).[12] The tests conducted by Aragon et al.[9–11] sought to establish a rigorous seismic design methodology for connectors with shorter grouted lengths. The cyclic uniaxial loading tests showed that energy-dissipation bars in tapered connection ducts achieved the most ductile performance when a duct taper angle of 1.5 degrees was used. However, a taper is not necessary as long as a straight corrugated steel duct is used with a minimum bonded length of 12 times the bar diameter ($12d_{ED}$) for no. 7 and 9 (22M and 29M) energy-dissipation bars and 15 times the bar diameter ($15d_{ED}$) for no. 11 (36M) bars. These bonded lengths are much shorter than the bar development lengths required by ACI 318-19. Ultimately, Aragon et al.[11] recommended corrugated straight steel ducts over tapered ducts because corrugated straight steel ducts take up less space in the wall cross section, are readily available, and are more cost effective.

This paper builds on and further develops the knowledge and validation for the use of short-grouted corrugated steel duct connectors for energy-dissipation reinforcing bars in seismic precast concrete construction. Specifically, whereas previous testing by Aragon et al. was limited to single connectors under uniaxial loading, the focus of the current paper is the performance of these connectors, including group and edge effects, in precast concrete shear walls tested under reversed-cyclic lateral loading in accordance with the validation requirements of ACI 550.6-19[7] and ACI 318-19[2] section 18.11.2.2.

Test specimen design and details

Three shear wall specimens were designed, constructed, and tested.[7] Each specimen included a single precast concrete wall panel connected to a reinforced concrete foundation along a horizontal joint. The wall panels for the three specimens were 66 in. (1676 mm) long, 150 in. (3810 mm) high, and 15.5 in. (394 mm) thick, while each foundation was 96 in. (2438 mm) long, 32 in. (813 mm) high, and 56 in. (1422 mm) wide. The reinforcement cage and formwork for the wall panel and foundation for specimen 1 were constructed in California and shipped to the Structural Systems Laboratory at the University of Notre Dame, in Indiana, for concrete casting and testing. The wall panel and foundation components for specimen 2 were produced in California and the components for specimen 3 were produced in South Carolina and shipped to the University of Notre Dame for testing.

Following the recommendation by Aragon et al.,[11] straight corrugated steel ducts were used as the connector ducts for the energy-dissipation bars. The connector ducts were placed in the wall panel rather than inside the foundation. This choice was made to create more critical conditions for performance testing of the connectors since the wall panel was thinner and provided less confinement to the connector ducts than the much larger foundation. The wall panel was also expected to receive more significant damage in the form of concrete cracking and crushing, resulting in reduced confinement around the connectors under lateral loading. To establish the wall-to-foundation connection in all three specimens, ASTM A706[6] Grade 60 (414 MPa), no. 11 (36M) energy-dissipation bars were embedded and fully anchored inside the foundation (using headed ends at the bottom of the bars) and grouted inside the ducts at the bottom of the wall panel. A 1 in. (25 mm) thick horizontal grout pad was used between the wall and the foundation for tolerance and alignment at the interface. The energy-dissipation bars were intentionally unbonded (by wrapping the bars inside a thin plastic sleeve) within this horizontal grout pad (base pad) to limit damage to the grout pad by transferring the bar forces above and below the pad rather than within the pad.

Design of connector tie reinforcement

Steel tie reinforcement was designed around the short-grouted duct connectors to transfer the energy-dissipation bar forces into the wall panel. The tie reinforcement comprised vertical (along the wall height), transverse (along the wall thickness), and longitudinal (along the wall length) ASTM A706 bars. The steel area for each tie component was calculated based on the strut-and-tie model (**Fig. 1**) developed by Aragon et al.[8] The vertical ties were designed to yield when the energy-dissipation bars yield in order to spread the yielding of flexural reinforcement into the wall panel and reduce the concentration of yielding at the wall-to-foundation joint interface. The total required area of vertical tie reinforcement A_{vt} to transfer the total tension force in the energy-dissipation bars T_{ED} placed in a single layer across the wall thickness was calculated using:

$$A_{vt} = \frac{A_{ED} \cdot f_{y,ED}}{f_{y,vt}}$$

where

A_{ED} = total area of energy-dissipation bar or bars placed in one layer across the thickness of the wall (Fig. 1 shows a single energy-dissipation bar across the thickness of a wall)

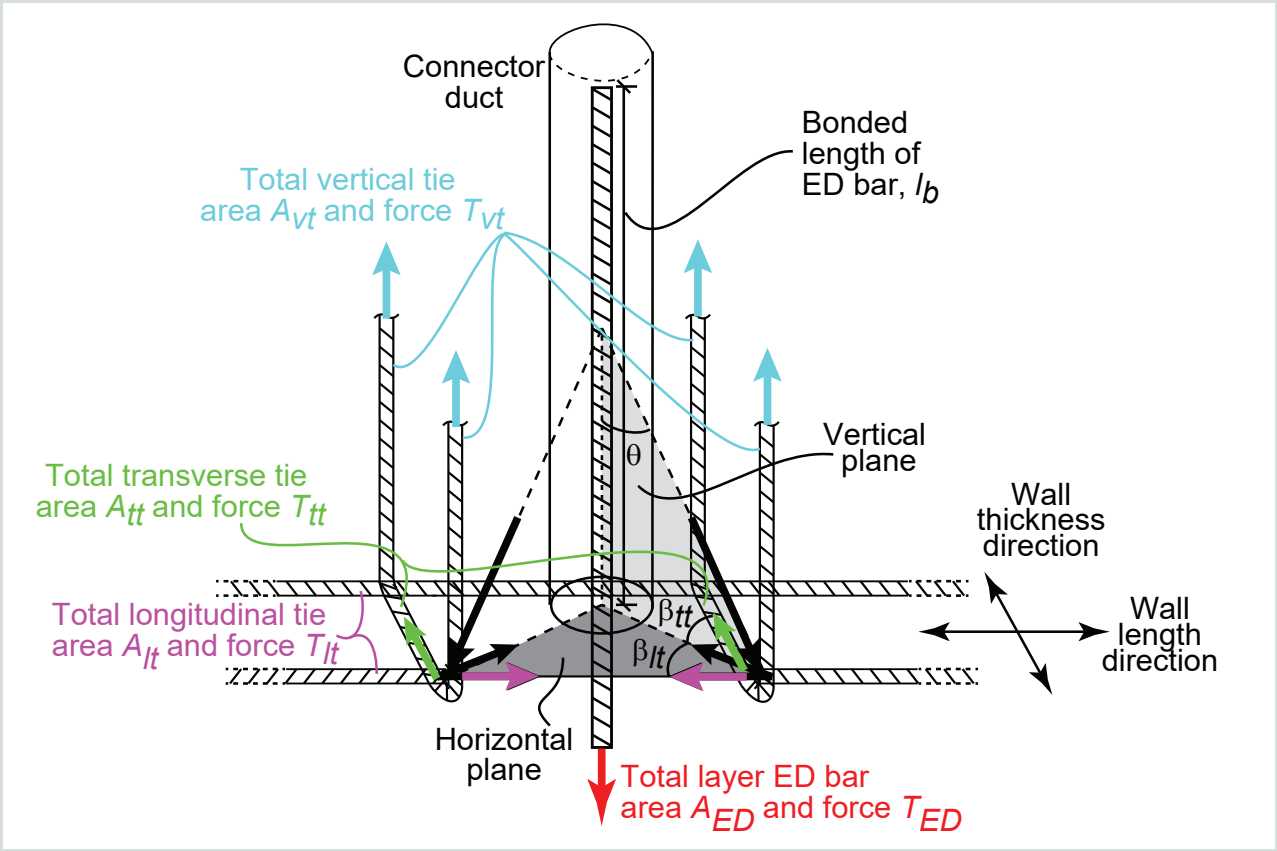

Figure 1. Strut-and-tie model. Source: Adapted from Aragon, T. A., Y. C. Kurama, and D. F. Meinheit, "A Type III Grouted Seismic Connector for Precast Concrete Structures," *PCI Journal* 62 (5): pp. 75–88.
Note: ED = energy-dissipation. ℓ_b = bonded length of energy-dissipation bar; T_{ED} = total tension force in energy-dissipation bar or bars placed in one layer across thickness of wall; T_{lt} = total tension force in longitudinal tie reinforcement designed as part of strut-and-tie model; T_{tt} = total tension force in transverse tie reinforcement designed as part of strut-and-tie model; T_{vt} = total tension force in vertical tie reinforcement designed to transfer T_{ED} to wall; $\beta_{\ell t}$ = angle of horizontal plane in strut-and-tie model of connector tie reinforcement; θ = angle of vertical plane in strut-and-tie model.

$f_{y,ED}$ = yield strength of the energy-dissipation bars

$f_{y,vt}$ = yield strength of the vertical tie bars

The transverse and longitudinal tie reinforcing bars were designed to not yield until the attainment of the ultimate (peak) strength of the energy-dissipation bars. This design choice was made to limit the amount of vertical cracking near the base of the wall panel so that the concrete can provide effective confinement around the connectors. The total required area of transverse tie reinforcement A_{tt} and the total required area of longitudinal tie reinforcement $A_{\ell t}$, designed as part of the strut-and-tie model, were calculated using:

$$A_{tt} = \frac{A_{vt} \cdot f_{u,vt} \cdot \tan(\theta)}{2 \cdot f_{y,tt} \cdot \cos(\beta_{tt})}$$

where

$f_{u,vt}$ = ultimate (peak) strength of the vertical tie bars

θ = vertical plane angle of the strut-and-tie model (Fig. 1)

$f_{y,tt}$ = yield strength of the transverse tie bars

β_{tt} = horizontal plane angle (Fig. 1)

$$A_{\ell t} = \frac{A_{vt} \cdot f_{u,vt} \cdot \tan(\theta)}{2 \cdot f_{y,\ell t} \cdot \cos(\beta_{\ell t})}$$

where

$f_{y,\ell t}$ = yield strength of the longitudinal tie bars

$\beta_{\ell t}$ = horizontal plane angle (Fig.1, complementary angle to β_{tt})

The vertical tie reinforcement area A_{vt}, transverse tie reinforcement area A_{tt}, and longitudinal tie reinforcement area $A_{\ell t}$ should be provided symmetrically around each layer of energy-dissipation bars along the thickness and length of the wall, and should be adequately developed. The required vertical and transverse tie reinforcement areas between two adjacent layers of energy-dissipation bars can be combined. In the strut-and-tie model, $\beta_{\ell t}$ and β_{tt} are complementary angles and can be calculated based on the layout of the tie and energy-dissipation reinforce-

ment in the wall cross section. In all three specimens, $\beta_{\ell t}$ was approximated as 45 degrees ($\beta_{\ell t} = \beta_{tt} = 45$ degrees). The angle θ can be calculated based on the layout of the tie reinforcement and an estimated work point on the bonded length of the energy-dissipation bar. In specimen 1, θ was taken as 30 degrees, and in specimens 2 and 3, it was taken as 25 degrees.

Specimen 1

The cross-section view in **Fig. 2** presents the reinforcement details at the base of the specimen 1 wall panel, which had 16 no. 11 (36M) energy-dissipation bar connectors distributed symmetrically about the mid-length and mid-thickness of the panel. Of the 16 energy-dissipation bars, 14 had a bonded length of 15 times the energy-dissipation bar diameter, $15d_{ED}$, and the other 2 bars, which were located at the outermost northern layer, had a longer bonded length of $18d_{ED}$ (Fig. 2). The $15d_{ED}$ bonded length was consistent with the findings of Aragon et al.[10] for no. 11 (36M) energy-dissipation bars, and the $18d_{ED}$ connector length was selected as a testing variable.

Two no. 8 (25M) ASTM A706[6] Grade 60 (414 MPa) headed bars spaced at 3 in. (76 mm) were placed next to each connector as the vertical tie reinforcement. The transverse tie reinforcement consisted of three layers (vertically spaced at 4 in. [102 mm] along the height of the connectors) with four no. 5 (16M) rectilinear reinforcing bars (tie bar 1 and tie bar 2) in each layer. Tie bar 1 was ASTM A706 Grade 60, and tie bar 2 was ASTM A706 Grade 80 (552 MPa). The legs of tie bars 1 and 2 running in the thickness direction of the wall were considered to be the transverse ties. In addition to the legs of these two tie bars running in the length direction of the wall, no. 5 reinforcing bars with 180 degree hooks were used as the longitudinal tie reinforcement. This reinforcement consisted of three layers of ASTM A706 Grade 80 outer longitudinal bars and two layers of ASTM A706 Grade 60 inner longitudinal bars (Fig. 2). Tie bars 1 and 2 and the hooked longitudinal bars were continued at 8 in. (203 mm) spacing along the height of the wall above the connector region. Generally, even though the wall reinforcement could be reduced above the connector region, these upper region

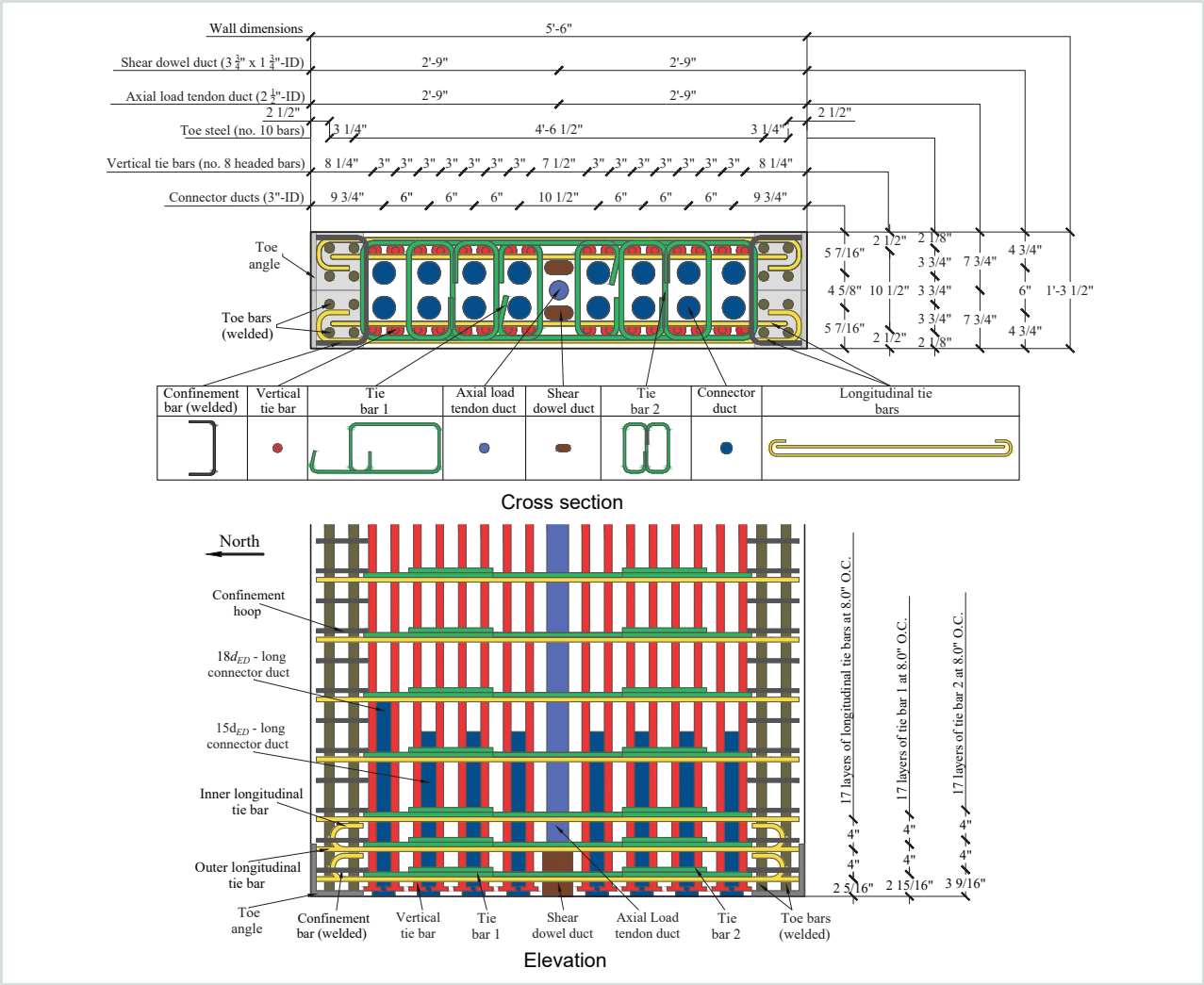

Figure 2. Base of specimen 1 wall panel. Note: d_{ED} = diameter of energy-dissipation bar; ID = inner diameter; O.C. = on center. No. 8 = 25M; no. 10 = 32M; 1" = 1 in. = 25.4 mm; 1' = 1 ft = 0.305 m.

details were deemed to have insignificant effect on the wall performance. As such, reinforcement changes above the connectors were minimized to ease specimen shop drawings and fabrication.

The design of specimen 1 included additional considerations that exceeded ACI 318-19[2] requirements to allow the wall to undergo large nonlinear base rotations without shear or concrete compression failure so that the connectors could be tested up to large nonlinear tension strains of the energy-dissipation bars. Specifically, two shear dowels were placed at the mid-length of the wall base to reduce the relative slip displacement between the wall and the foundation (wall base sliding). Furthermore, at each toe of the wall panel, one no. 4 (13M) ASTM A706 Grade 60 (414 MPa) U-shaped transverse bar and eight no. 10 (32M) ASTM A706 Grade 60 compression-only vertical steel bars were welded to a steel angle to prevent concrete crushing. The compression-only bars did not cross the base joint and, thus, did not contribute to the lateral strength of the wall. Concrete confinement above the welded U-shaped bar at each toe was provided by no. 4 ASTM A706 Grade 60 closed hoops spaced at 4 in. (102 mm) along the wall height.

Specimen 2

The design and detailing of specimen 2 were altered significantly based on the unsatisfactory measured and observed performance of specimen 1 described in the results section of this article. The connector ducts in specimen 2 were sized to accommodate $15d_{ED}$ bonded length of the no. 11 (36M) energy-dissipation bars projecting from the foundation. The energy-dissipation bars were moved closer to the wall toes, and the steel angles and compression-only bars used at the toes of specimen 1 were eliminated in specimen 2 (**Fig. 3**). The vertical and transverse tie reinforcement were provided by no. 8 (25M) ASTM A706 Grade 60 (414 MPa) U bars placed on both sides of the connectors, where the vertical legs of the U bars served as the vertical tie reinforcement and the horizontal legs served as the transverse tie reinforcement.

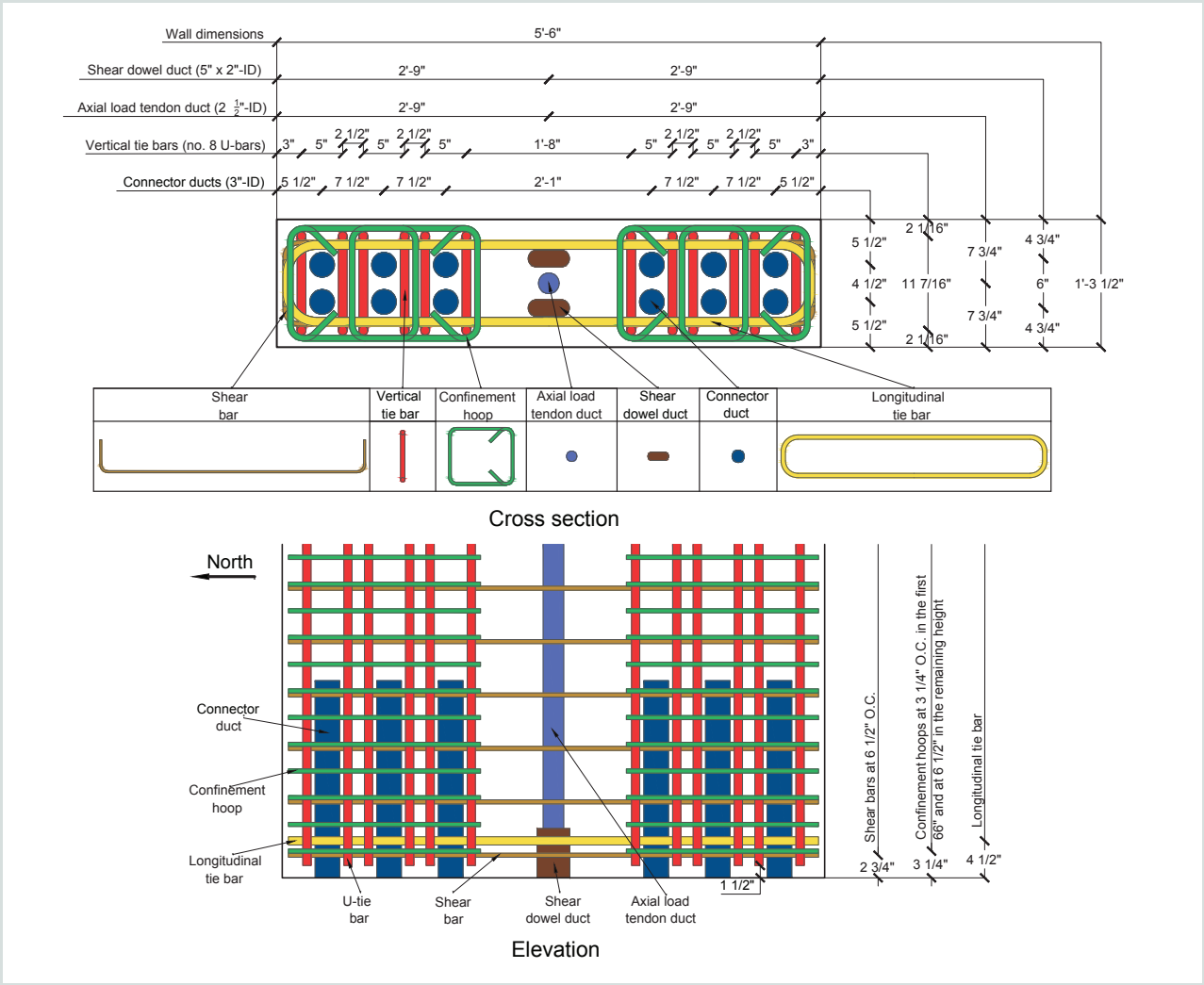

Figure 3. Base of specimen 2 wall panel. Note: ID = inner diameter; O.C. = on center. No. 8 = 25M; 1" = 1 in. = 25.4 mm; 1' = 1 ft = 0.305 m.

The purpose for selecting U bars for the vertical and transverse ties was to better engage the wall thickness in transferring the energy-dissipation bar forces to the tie reinforcement. Similarly, a single closed no. 8 (25M) ASTM A706 Grade 60 (414 MPa) hoop was placed around the entire wall perimeter (Fig. 3) to serve as the longitudinal tie reinforcement. The transverse reinforcement at the toes of the wall was designed in accordance with the special boundary region requirements in ACI 318-19[2] section 18.10.6.4. This boundary reinforcement included two no. 4 (13M) ASTM A706 Grade 80 (552 MPa) overlapping hoops spaced at 3¼ in. (83 mm) for the first 66 in. (1676 mm) of the wall height (that is, over a height equal to the wall length), and spaced at 6½ in. (165 mm) for the remaining height of the wall. Shear reinforcement was provided by no. 4 ASTM A706 Grade 80 hooked bars spaced at 6½ in. throughout the height of the wall in accordance with ACI 318-19 section 18.10.4.1. As in specimen 1, two shear dowels were installed in specimen 2 to limit shear slip (base sliding) at the wall-to-foundation joint interface.

Specimen 3

The schematic diagrams in **Fig. 4** illustrate the reinforcement layout at the base of the wall for specimen 3. This specimen was identical to specimen 2, except for minor changes based on the measured and observed performance of specimen 2 described in the results section of this article. The first alteration was the reduction of concrete cover to the tie reinforcement. The bottommost tie reinforcement in specimen 2 (Fig. 3) was the horizontal legs of the U bars, and the clear cover distance to this reinforcement from the bottom of the wall was 1½ in. (38 mm). In specimen 3, this cover was reduced to ¾ in. (19 mm), which is the minimum cover for shear wall reinforcement specified in ACI 318-19.[2] Furthermore, the first layer of confinement hoops was placed at the same level (Fig. 4). Reducing the concrete cover was intended to improve the effectiveness of the confinement and tie reinforcement around the energy-dissipation bar connectors.

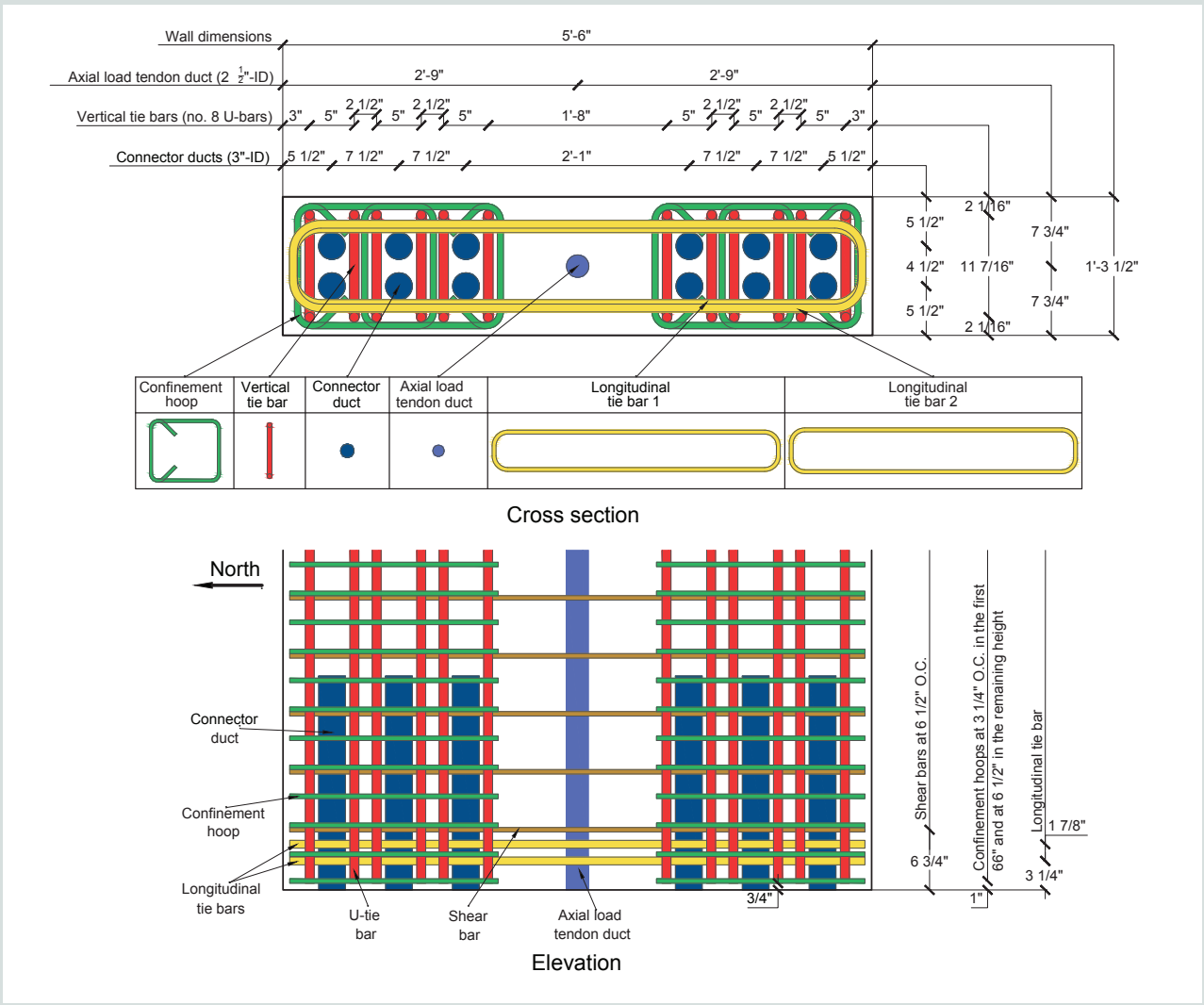

Figure 4. Base of specimen 3 wall panel. Note: ID = inner diameter; O.C. = on center. No. 8 = 25M. 1" = 1 in. = 25.4 mm; 1' = 1 ft = 0.305 m.

As a second modification in specimen 3, the longitudinal tie reinforcement area was increased. Whereas the area in specimen 2 was 0.79 in.^{2} (20 mm^2), composed of a single layer of no. 8 (25M) bars, the area in specimen 3 was 1.2 in.^{2} (31 mm^2), composed of two layers of no. 7 (22M) bars. The third change was to intentionally unbond the energy-dissipation bars over an additional length of $3d_{ED}$ right above the 1 in. (25 mm) unbonded length within the base joint grout pad, while maintaining the $15d_{ED}$ length of the energy-dissipation bars within the connectors above the grout pad ($3d_{ED}$ unbonded length plus $12d_{ED}$ bonded length). As a final modification, the shear dowels were removed. The reasons for making the modifications in specimen 3 are described later as part of the measured test results for specimen 2.

The foundation in each specimen was sized to accommodate the layout of the tie-down locations in the laboratory strong floor. A numerical analysis model was used to determine the maximum shear force and moment transferred to the foundation during the lateral loading of the wall. The steel reinforcement in the foundation was designed according to these maximum forces.

Test setup

Each wall specimen was tested using the setup shown in **Fig. 5**. A reversed-cyclic lateral load was applied using a servo-controlled hydraulic actuator with a 15 in. (381 mm) stroke and a capacity of 1600 kip (7117 kN). The centerline of the actuator was positioned 11 ft (3.3 m) from the base of the wall (top of the base grout pad) to create a base moment–to–shear ratio M_b/V_b of $2.0\ell_w$, where M_b is the base moment of the wall specimen, V_b is the base shear of the wall specimen, and ℓ_w is the wall length. In addition, a near-constant external axial load of 100 kip (445 kN) was applied using a vertically oriented, multistrand, unbonded post-tensioning tendon (which was placed inside a vertical duct at the center of the wall cross section) and a 220 kip (981 kN) capacity, center-hole hydraulic jack placed at the top of the wall. Including the self-weight of the wall panel, which was approximately 15 kip (67 kN), the total axial load ratio, $P/\left(f'_c A_g\right)$, was 0.019 at the base of each wall, where P is the total axial load, f'_c is the specified concrete compression strength, and A_g is the gross area of the wall section.

The foundation was elevated on two supporting concrete blocks to anchor the axial-load post-tensioning strands under the foundation. The foundation, lateral-load reaction wall, and end block were clamped to the strong floor of the laboratory using 1 in. (25 mm) diameter threaded steel rods. In addition, the foundation was horizontally post-tensioned to the lateral-load reaction wall and the end block using 0.6 in. (15 mm) diameter unbonded strands to create a stiff, self-reacting load application system with minimal sliding and uplifting.

To restrain the wall specimen from moving out of plane during the in-plane lateral-load testing, a steel frame was built around the wall. This steel frame was composed of columns, beams, diagonal braces, and plates. Two plates were connected to each north-south beam and extended to within

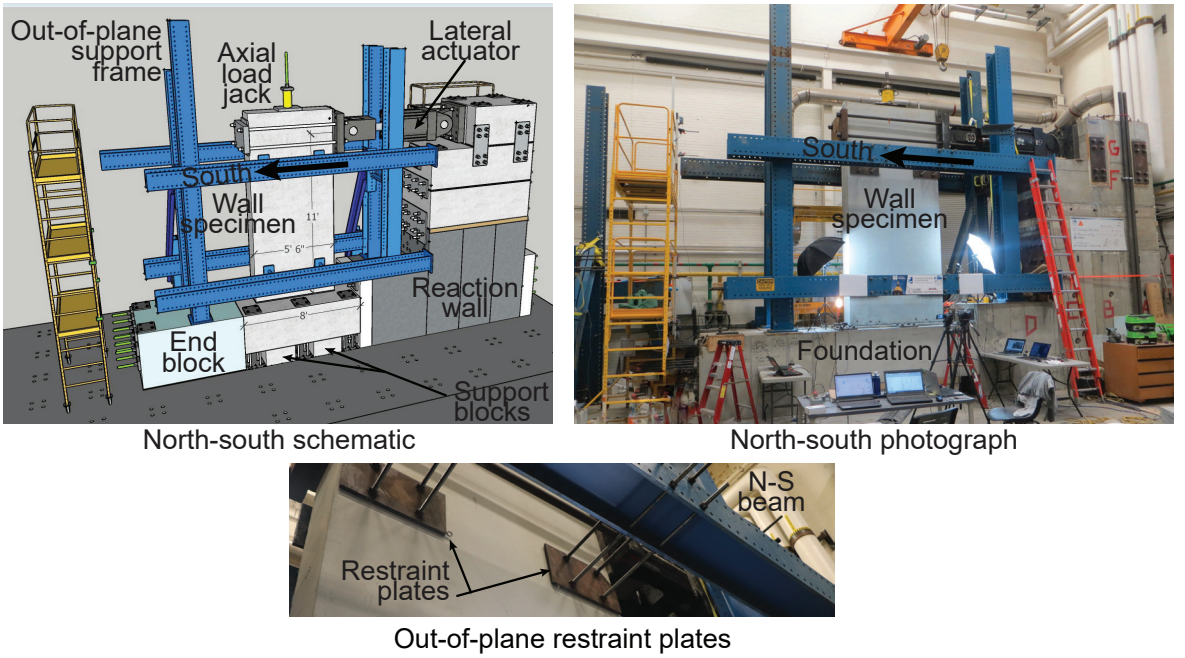

Figure 5. Test setup. Note: N-S = north-south.

a ¼ in. (6 mm) gap from the wall surfaces using threaded rods to provide out-of-plane restraint to the wall (Fig. 5). The surfaces of these plates were greased to minimize friction if the wall came into contact with the plates during the in-plane lateral-load testing.

Material properties

Reinforcing steel

Three samples for each reinforcing bar size in the three wall specimens were tested in a universal testing machine following ASTM A370, *Standard Test Methods and Definitions for Mechanical Testing of Steel Products*,[13] to determine the mechanical properties of the steel. All reinforcement was ASTM A706[6] Grade 60 or 80 (414 or 552 MPa). The bar strains up to the ultimate (peak) strength were measured using an extensometer with a gauge length of 2 in. (51 mm). After 0.5% drop in stress from the ultimate (peak) strength, the extensometer was removed and the additional bar strains were calculated from the subsequent relative movement of the testing machine crossheads. The bar stresses were calculated as the load recorded by the internal load cell of the testing machine divided by the nominal area of the bar. **Table 1** lists the measured steel modulus of elasticity E_s, yield strength f_y, yield strain ε_y, ultimate (peak) strength f_u, strain at ultimate (peak) strength (uniform elongation strain) ε_u, and strain at bar fracture ε_{fr}.

Connector ducts

Table 2 provides the dimensions of the connector ducts used in the three specimens. The connector ducts were straight corrugated steel ducts cut to length from post-tensioning ducts commonly available in the construction industry. The 3 in. (76 mm) inner diameter was selected to provide sufficient tolerance around the no. 11 (36M) energy-dissipation bars while placing the precast concrete wall on top of the foundation. Even though the connection ducts were provided by the same duct manufacturer, there were differences in the measured corrugation dimensions for the three specimens.

Concrete

In specimen 1, the batch of concrete used to cast the foundation was different from that used to cast the wall panel. However, in specimens 2 and 3, a single batch (one batch per specimen) was used to cast both the foundation and wall panel. The specified concrete compression strength for all three specimens was 6 ksi (41 MPa). A set of 3 × 6 in. (76 × 152 mm) concrete cylinders were cast to measure the modulus of elasticity E_c, from compression tests in accordance with ASTM C469, *Standard Test Method for Static Modulus of Elasticity and Poisson's Ratio of Concrete in Compression*[14]; compression strength f'_c, in accordance with ASTM C39, *Standard Test Method for Compressive Strength of Cylindrical Concrete Specimens*[15]; and split cylinder tension strength f_t, in accordance with ASTM C496, *Standard Test Method for Splitting Tensile Strength of Cylindrical Concrete Specimens*.[16] In addition, 6 × 6 × 18 in. (152 × 152 × 457 mm) modulus of rupture beams were cast to measure the flexural tension strength of the concrete in accordance with ASTM C293, *Standard Test Method for Flexural Strength of Concrete (Using Simple Beam With Center-Point Loading)*.[17] All concrete samples were kept in a moist environment until tested. **Table 3** presents the average measured concrete properties from three material samples. The concrete modulus of elasticity was calculated from strains measured using an averaging extensometer with 2 in. (51 mm) gauge length.

Grout

Commercially available, premixed (bagged) cementitious grout was used in the energy-dissipation bar connector ducts and to create a horizontal pad (base pad) at the interface between the wall panel and the foundation. The grout products were the same as those used and identified by Aragon et al.[9,10] as GM1, GM2, and GM3. Grout GM1 was used to create the horizontal grout pad at the base joint of all three specimens. Polypropylene fibers were added to the base pad grout mixture in specimens 1 and 2 per the fiber manufacturer's recommended dosage of 1.0 lb/yd^3 (0.59 kg/m^3). In specimen 1, the wall panel was lowered on top of freshly placed grout mixed in a plastic consistency per the manufacturer's recommendation to form the horizontal grout pad. In specimens 2 and 3, the wall panel was aligned on top of 1 in. (25 mm) thick wooden shims, and grout mixed in a fluid consistency according to manufacturer's recommendations was manually pumped under the wall to create the grout pad.

The grout material used in the connector ducts in specimens 2 and 3 was GM3, which was identified by Aragon et al.[10] as the lowest-performing grout. In specimen 1, different grout products were used in each connector duct (**Fig. 6**). To simulate possible field construction errors, the connector grout used in specimen 1 was mixed with 5% more water than the maximum amount recommended by the manufacturer for fluid consistency. In specimens 2 and specimen 3, the grout for the connector ducts was mixed with the maximum amount of water recommended by the manufacturer for fluid consistency. The connector grout for all three specimens was manually pumped into the ducts through a grout-in tube placed near the bottom of each duct until grout flowed from a grout-out tube near the top of the duct.

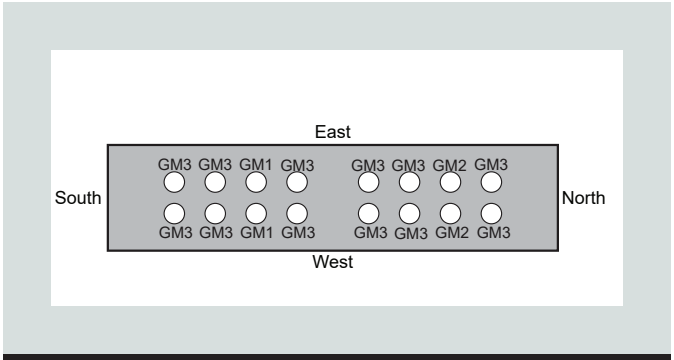

Figure 6. Wall cross-section view showing grout materials (GM) used in the connector ducts of specimen 1.

Table 1. Reinforcing steel properties

		Specimen 1	Specimen 2	Specimen 3
Energy dissipation	Bar size (Grade)	no. 11 (60)	no. 11 (60)	no. 11 (60)
	E_s, ksi	27,613	28,154	27,291
	$f_{y,ED}$, ksi	63.12	64.81	66.98
	$\varepsilon_{y,ED}$, in./in.	0.0037	0.0026	0.0031
	$f_{u,ED}$, ksi	99.23	96.15	89.39
	$\varepsilon_{u,ED}$, in./in.	0.1086	0.1096	0.1258
	$\varepsilon_{fr,ED}$, in./in.	0.196	0.198	0.196
Longitudinal tie	Bar size (Grade)	no. 5 (60 and 80)	no. 8 (60)	no. 7 (60)
	E_s, ksi	27,389/25,866	27,476	28,503
	$f_{y,lt}$, ksi	62.82/83.09	63.52	69.67
	$\varepsilon_{y,lt}$, in./in.	0.0034/0.0037	0.0027	0.0026
	$f_{u,lt}$, ksi	93.18/111.5	93.42	97.71
	$\varepsilon_{u,lt}$, in./in.	0.1127/0.0912	0.1084	0.1161
	$\varepsilon_{fr,lt}$, in./in.	0.199/0.165	0.181	0.192
Vertical tie	Bar size (Grade)	no. 8 (60)	no. 8 (60)	no. 8 (60)
	E_s, ksi	28,082	27,476	24,885
	$f_{y,vt}$, ksi	65.57	63.52	63.34
	$\varepsilon_{y,vt}$, in./in.	0.0029	0.0027	0.0035
	$f_{u,vt}$, ksi	94.84	93.42	94.29
	$\varepsilon_{u,vt}$, in./in.	0.1156	0.1084	0.1169
	$\varepsilon_{fr,vt}$, in./in.	0.208	0.181	0.202
Transverse tie	Bar size (Grade)	no. 5 (60 and 80)	no. 8 (60)	no. 8 (60)
	E_s, ksi	27,389/25,866	27,476	24,885
	$f_{y,tt}$, ksi	62.82/83.09	63.52	63.34
	$\varepsilon_{y,tt}$, in./in.	0.0034/0.0037	0.0027	0.0035
	$f_{u,tt}$, ksi	93.18/111.5	93.42	94.29
	$\varepsilon_{u,tt}$, in./in.	0.1127/0.0912	0.1084	0.1169
	$\varepsilon_{fr,tt}$, in./in.	0.199/0.165	0.181	0.202
Confinement hoop	Bar size (Grade)	no. 4 (60)	no. 4 (80)	no. 4 (80)
	E_s, ksi	n.d.	25,758	24,431
	$f_{y,c}$, ksi	68.90	86.49	86.71
	$\varepsilon_{y,c}$, in./in.	n.d.	0.0053	0.0056
	$f_{u,c}$, ksi	99.60	115.4	116.1
	$\varepsilon_{u,c}$, in./in.	n.d.	0.0801	0.0939
	$\varepsilon_{fr,c}$, in./in.	n.d.	0.122	0.143

Note: n.d. = no data; E_s = modulus of elasticity of reinforcing bar; $f_{u,c}$ = ultimate (peak) strength of confinement hoop bars; $f_{u,ED}$ = ultimate (peak) strength of energy-dissipation bars; $f_{u,lt}$ = ultimate (peak) strength of longitudinal tie bars; $f_{u,tt}$ = ultimate (peak) strength of transverse tie bars; $f_{u,vt}$ = ultimate (peak) strength of vertical tie bars; $f_{y,c}$ = yield strength of confinement hoop bars; $f_{y,ED}$ = yield strength of energy-dissipation bars; $f_{y,lt}$ = yield strength of longitudinal tie bars; $f_{y,tt}$ = yield strength of transverse tie bars; $f_{y,vt}$ = yield strength of vertical tie bars; $\varepsilon_{fr,c}$ = strain at fracture of confinement hoop bars; $\varepsilon_{fr,ED}$ = strain at fracture of energy-dissipation bars; $\varepsilon_{fr,lt}$ = strain at fracture of longitudinal tie bars; $\varepsilon_{fr,tt}$ = strain at fracture of transverse tie bars; $\varepsilon_{fr,vt}$ = strain at fracture of vertical tie bars; $\varepsilon_{u,c}$ = strain at ultimate (peak) strength of confinement hoop bars; $\varepsilon_{u,ED}$ = strain at ultimate (peak) strength of energy-dissipation bars; $\varepsilon_{u,lt}$ = strain at ultimate (peak) strength of longitudinal tie bars; $\varepsilon_{u,tt}$ = strain at ultimate (peak) strength of transverse tie bars; $\varepsilon_{u,vt}$ = strain at ultimate (peak) strength of vertical tie bars; $\varepsilon_{y,c}$ = yield strain of confinement hoop bars; $\varepsilon_{y,ED}$ = yield strain of energy-dissipation bars; $\varepsilon_{y,lt}$ = yield strain of longitudinal tie bars; $\varepsilon_{y,tt}$ = yield strain of transverse tie bars; $\varepsilon_{y,vt}$ = yield strain of vertical tie bars. No. 4 = 13M; no. 5 = 16M; no. 7 = 22M; no. 8 = 25M; no. 11 = 36M; 1 in. = 25.4 mm; 1 ksi = 6.895 MPa.

Table 2. Connector duct dimensions

	Specimen 1	Specimen 2	Specimen 3
Inner diameter, in.	3.0	3.0	3.0
Outer diameter, in.	3.125	3.125	3.125
Thickness, in.	0.02	0.02	0.02
Corrugation height, in.	0.04	0.07	0.07
Corrugation width, in.	0.22	0.34	0.19
Corrugation spacing, in.	0.51	0.93	0.51

Note: 1 in. = 25.4 mm.

Table 3. Concrete properties

Specimen		$E_{c,td}$, ksi	$f'_{c,28d}$, ksi	$f'_{c,td}$, ksi	$f_{t,28d}$, ksi	$f_{t,td}$, ksi	$f_{r,28d}$, ksi	$f_{r,td}$, ksi
1	Wall	6471	7.5	8.4	0.711	0.811	n.d.	0.797
	Foundation	6066	8.0	9.0	0.793	0.964	n.d.	0.798
2	Wall	3830	5.6	6.8	0.674	0.741	0.729	0.735
	Foundation							
3	Wall	2496	6.8	7.3	0.727	0.787	0.877	0.870
	Foundation							

Note: n.d. = no data; $E_{c,td}$ = modulus of elasticity of concrete at wall test day; $f_{r,td}$ = modulus of rupture of concrete at test day; $f_{r,28d}$ = modulus of rupture of concrete at 28 days; $f_{t,td}$ = split cylinder tension strength of concrete at test day; $f_{t,28d}$ = split cylinder tension strength of concrete at 28 days; $f'_{c,td}$ = compression strength of concrete at test day; $f'_{c,28d}$ = compression strength of concrete at 28 days. 1 ksi = 6.895 MPa.

Table 4 presents the water-to-grout weight ratio *w*/*g* as well as the spread, modulus of elasticity E_{cg}, compression strength f'_{cg}, and split cylinder tension strength f_{tg} of the grout. The flowability of each grout mixture was measured as the lateral flow diameter (spread) of freshly mixed grout on top of a smooth, nonabsorbent plastic plate after slowly lifting a 2 in. (51 mm) diameter, 4 in. (102 mm) tall plastic tube filled with grout. The compression strength was measured by testing 2 × 2 in. grout cubes in accordance with ASTM C109, *Standard Test Method for Compressive Strength of Hydraulic Cement Mortars (Using 2-in. or [50-mm] Cube Specimens)*.[18] To measure the modulus of elasticity and tension strength of the grout, 3 × 6 in. (76 × 152 mm) grout cylinders were tested in accordance with ASTM C469[14] and ASTM C496,[16] respectively.

Instrumentation

Forces, displacements, rotations, and strains were recorded during the testing of each specimen. Pressure transducers were used to measure the applied axial and lateral loads. In-plane and out-of-plane displacements and deformations of the wall and the foundation were recorded using a set of string potentiometers installed on and around the specimen (**Fig. 7**). The in-plane displacements included the lateral displacement of the wall at the line of lateral loading (centerline of the lateral actuator), the lateral displacement of the wall base with respect to the foundation (wall base sliding), and the lateral displacement of the foundation (foundation sliding). To monitor the out-of-plane displacements, four string potentiometers were connected to the wall and two were connected to the foundation. Diagonally and vertically oriented string potentiometers were attached to the wall to measure the shear and flexural deformations, respectively. Linear variable displacement transducers placed across the base joint interface were used to measure the rotation and neutral axis location at the base of the wall.

To measure the initiation and progression of yielding in the energy-dissipation bars, strain gauges were installed at the mid-length of the unbonded region of select bars in all three specimens (½ in. [13 mm] above the top of the foundation for specimens 1 and 2, and 2⅝ in. [67 mm] above the top of the foundation for specimen 3). The energy-dissipation bars in specimens 2 and 3 were also strain gauged 3 in. (76 mm) below the top of the foundation. Moreover, to understand the effectiveness of the tie reinforcement around the energy-dissipation bar connectors, strain gauges were installed on select longitudinal, vertical, and transverse ties. Layouts of the strain gauges for the three specimens are shown in **Fig. 8**. The exact location and number of strain gauges varied from specimen to specimen depending on the design and detailing of the reinforcement. All strain gauges were installed on reinforcing bars near the west face of the wall, which was the open casting surface as shown in the photograph in Fig. 8 (the west bars

Table 4. Grout properties

Specimen	Location	Grout product	*w/g*	Spread, in.	$E_{cg,td}$, ksi	$f'_{cg,28d}$, ksi	$f'_{cg,td}$, ksi	$f_{tg,28d}$, ksi	$f_{tg,td,}$ ksi
1	Base pad	GM1	0.164	n.d.	3605	7.13	6.73	0.723	0.531
	Connector ducts	GM1	0.201	8.56	3221	6.48	6.50	0.522	0.859
		GM2	0.197	8.63	3125	5.81	5.59	0.397	0.713
		GM3 east	0.183	10.1	2980	5.09	5.11	0.460	0.773
		GM3 west	0.183	10.2	2945	4.84	4.68	0.371	0.679
2	Base pad	GM1	0.191	7.50	4247	10.4	10.7	0.876	0.816
	Connector ducts	GM3	0.174	11.6	4238	8.24	8.63	0.677	0.727
3	Base pad	GM1	0.191	6.75	3916	10.2	11.3	n.d.	n.d.
	Connector ducts	GM3	0.174	6.88	3598	8.52*		0.788*	

Note: n.d. = no data. $E_{cg,td}$ = modulus of elasticity of grout at wall test day; $f_{tg,td}$ = split cylinder tension strength of grout at wall test day; $f_{tg,28d}$ = split cylinder tension strength of grout at 28 days; $f'_{cg,td}$ = compression strength of grout at wall test day; $f'_{cg,28d}$ = compression strength of grout at 28 days; *w/g* = water-to-grout weight ratio. 1 in. 25.4 mm; 1 ksi = 6.895 MPa.

* Specimen 3 was tested 28 days after placement of grout in the connectors.

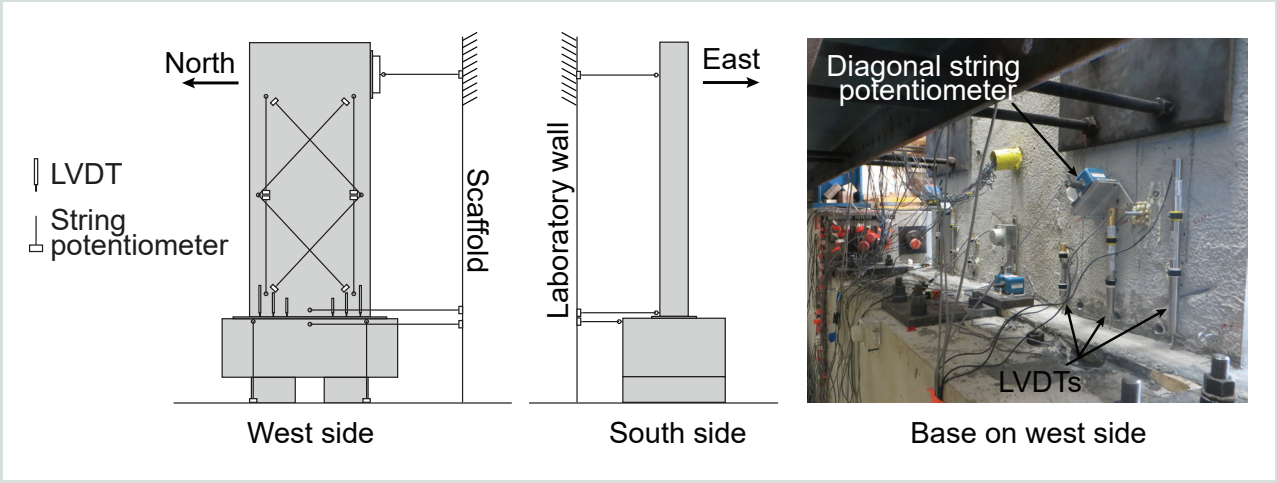

Figure 7. Instrument layout. Note: LVDT = linear variable displacement transducer.

were chosen because their surfaces were easier to access for strain gauge application inside the formwork).

Loading protocol

Testing of each wall specimen started with the application of the superimposed axial load followed by a load-controlled lateral loading series. Three fully reversed lateral-load cycles were applied at target loads of ±50, 100, 150, and 200 kip (±222, 445, 667, and 890 kN) (**Fig. 9**). The lateral loading started toward the south direction, which is referred to as the positive direction (with the actuator in compression). The second series of the lateral loading protocol was a displacement-controlled series in terms of lateral drift. Three fully reversed cycles were applied at each drift level, except for the last drift level (4.7% drift) during the testing of specimen 3; at that level, two cycles were applied. Each new lateral displacement amplitude was calculated as 1.5 times the previous displacement amplitude in accordance with ACI 550.6-19.[7] The actual displacement-controlled loading histories for specimens 1, 2 and 3 are shown in Fig. 9. Unlike specimen 1, the targeted drift levels applied on specimens 2 and 3 were back calculated from the ACI 550.6-19 validation-level drift of 2.1% for $M_b/V_b = 2.0\ell_w$.

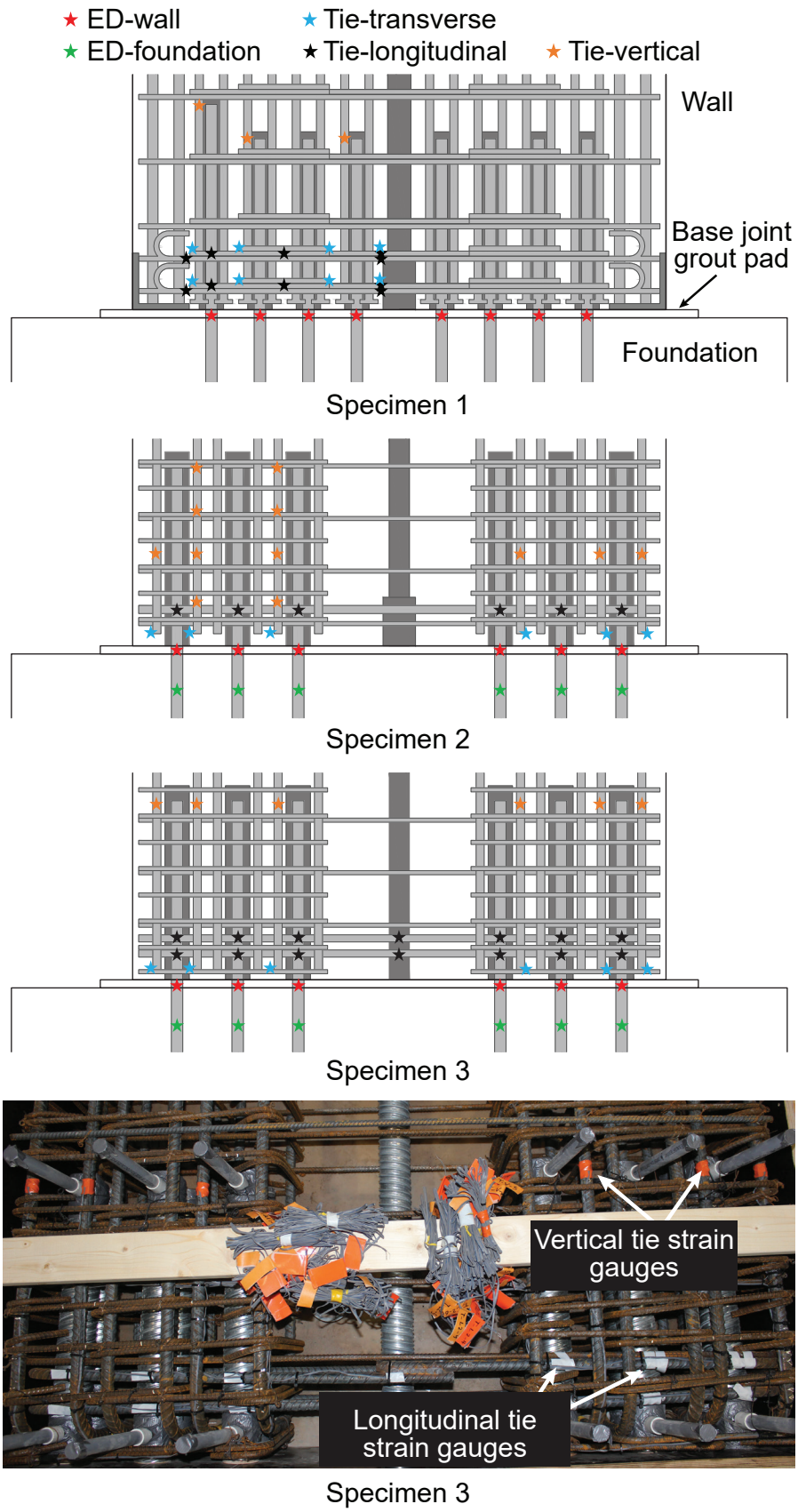

Figure 8. Strain gauge placement. Note: ED = energy-dissipation.

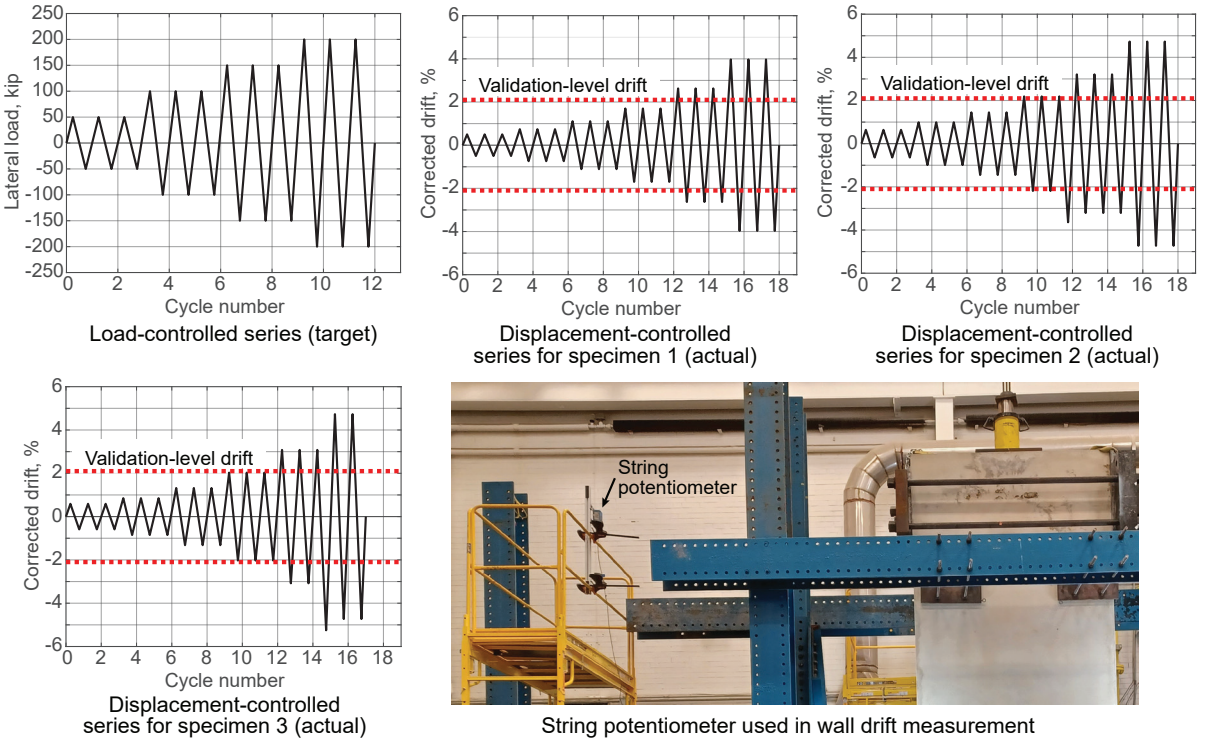

Figure 9. Lateral loading of test specimens. Note: 1 kip = 4.448 kN.

In the third negative-direction loading at the fourth drift level (validation-level drift), specimen 2 was displaced more than the target displacement in an attempt to reach the required strength specified by ACI 550.6-19 (less than 20% drop in strength from the overall peak strength in each direction). Specimen 3 was similarly displaced beyond the target displacement in the third negative-direction loading at the fifth drift level (3.1% drift). However, as discussed in the results section, neither specimen achieved the required strength during these increased lateral displacement cycles.

The wall drift was computed as the lateral displacement of the wall measured at the line of lateral loading divided by the height to the base grout pad (equal to 11 ft [3.3 m]). A string potentiometer mounted on a stationary scaffold at the same level as the centerline of the actuator was used to record the lateral displacement of the wall (Fig. 9). The wall drift was corrected for small amounts of sliding and rotation of the foundation, which were recorded using a set of string potentiometers placed on the foundation as discussed earlier in the instrumentation section.

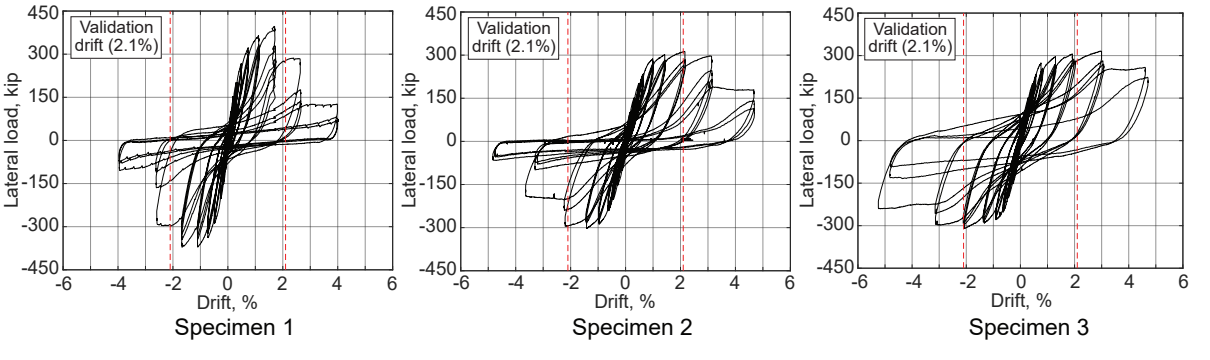

Figure 10. Lateral load-drift behavior. Note: 1 kip = 4.448 kN.

Results

Lateral load-drift behavior

Figure 10 presents the lateral load-drift behaviors of specimens 1, 2, and 3. For specimen 1, the peak (maximum) lateral strength V_{max} was slightly higher in the positive direction (loading toward the south) than in the negative direction (397 and 372 kip [1766 and 1655 kN], respectively, as noted in **Table 5**). This finding is typical of reversed-cyclic behavior of reinforced concrete structures where the strength is greater in the initial loading direction than in the reversed direction due to the accumulation of damage. Specimen 1 also had a longer bonded length of $18d_{ED}$ for the extreme north layer of energy-dissipation bars than the bonded length of all the other bars. The longer bonded length of the extreme north bars may have contributed to the greater strength of the wall by developing greater tension stresses when loading toward the south. Ultimate failure of specimen 1 was caused by breakout failure of the energy-dissipation bar connectors during the third cycle at 1.7% drift when the wall had 28% drop in load from the peak lateral strength V_{max} in the positive direction. This failure drift was smaller than, and did not satisfy, the ACI 550.6-19[7] validation-level drift requirement of 2.1%. Nonetheless, the drift performance of specimen 1 was better than that of specimen HW2 tested by Smith et al.,[2] which used commercial Type II grouted mechanical splices for the energy-dissipation bars.

Specimen 2 had smaller peak lateral strength (by about 25%) but performed much better than specimen 1. The larger lateral strength of specimen 1 as compared with specimens 2 and 3 was mostly because of the use of a larger total area of energy-dissipation bars (eight pairs in specimen 1 versus six pairs in specimens 2 and 3). In addition, the use of steel angles and compression-only bars at the toes of specimen 1 resulted in a smaller length of the wall base cross section in compression (which increased the lever arm for base moment resistance), as discussed in the neutral axis at wall base section of this article.

In the positive direction of loading, specimen 2 sustained three cycles at the validation-level drift of 2.1% with less than 20% strength loss and failed during the second cycle of the subsequent drift level (3.1%) with 21% strength loss. However, in the negative direction, the wall had a 33% drop in load (from the peak lateral strength V_{max}) during the third cycle to the validation-level drift (2.1%). As discussed in the loading protocol section, specimen 2 was displaced beyond 2.1% during this cycle, but instead of gaining strength, the wall experienced further reduction in strength (Fig. 10). Consequently, the wall was deficient by half a cycle from meeting the validation-level drift requirement of ACI 550.6-19.[7]

Comparing the hysteresis loops of specimens 1 and 2 in Fig. 10, the revised detailing of the tie reinforcement in specimen 2 enhanced the performance of the connectors. Notably, unlike the breakout failure of the connectors in specimen 1, the ultimate failure of specimen 2 was attributed to the concentration of concrete splitting, crushing, and loss of concrete confinement around the connectors, followed by the failure of the connectors. The evidence for this failure sequence is discussed in the neutral axis at wall base section later in the article.

Similar to specimen 2, specimen 3 achieved smaller peak lateral strength (by about 25%) as compared with specimen 1, but specimen 3 exhibited further improved performance as it sustained less than 20% strength loss at displacements beyond the validation-level drift. In the positive direction, the wall achieved a new peak lateral strength of 317 kip (1410 kN) and sustained three cycles at 3.1% drift and one additional cycle at the next drift level (4.7%) with less than 20% strength loss. In the negative direction, the peak lateral strength of 310 kip (1379 kN) was attained at the first cycle of the validation-level drift. Specimen 3 sustained three cycles at this drift level, plus two additional cycles at the next drift level (3.1%) with less than 20% load drop from the peak lateral strength recorded in the negative direction. The loss in strength was 23% during the third cycle at 3.1% drift, which was deemed the failure drift Δ_f for specimen 3.

The ratios of the peak measured lateral strengths of specimen 3 to the probable strength V_{pr} (calculated using the measured compression strength of unconfined concrete and measured nonlinear stress-strain relationship of the energy-dissipation bars) were 1.06 and 1.04 in the positive and negative directions, respectively (Table 5). These ratios are well within the

Table 5. Lateral load performance

Specimen	V_{max}, kip		Drift at V_{max}, %		Δ_f, % (cycle number)		Strength loss at failure, %		$\frac{V_{max}}{V_{pr}}$	
	(+)	(-)	(+)	(-)	(+)	(-)	(+)	(-)	(+)	(-)
1	397	372	1.7	1.7	1.7 (3)	2.6 (1)	28	21	1.14	1.07
2	314	303	2.1	1.4	3.1 (2)	2.1 (3)	21	33	1.03	1.00
3	317	310	3.0	2.1	4.7 (2)	3.1 (3)	30	23	1.06	1.04

Note: V_{max} = measured peak (maximum) lateral (base shear); Δ_f = failure drift; V_{pr} = probable lateral (base shear) strength calculated using measured compression strength of unconfined concrete and measured nonlinear stress-strain relationship of energy-dissipation bars. 1 kip = 4.448 kN.

ranges of 0.9 and 1.2 specified by ACI 550.6-19,[7] where a ratio greater than 1.0 indicates that the measured strength was greater than the calculated strength. The calculated probable strength was more accurate (that is, the peak measured lateral strength–to–probable strength ratios were closer to 1.0) for specimen 2 and less accurate (ratios as high as 1.14) for specimen 1. The ratios of the peak measured lateral strengths to the calculated probable strength were likely greater for specimen 1 because the probable strength calculation did not incorporate the steel angles or the compression-only bars used at the wall toes, which affected the neutral axis location at the wall base (and therefore, the lever arm used in the moment strength calculation). This point is discussed later in the neutral axis at wall base section of the article.

Progression of damage

Figure 11 presents damage photos for specimen 1 at the third cycle of the first displacement-controlled loading level (+0.53% drift), the failure drift level (+1.7%), and the last drift level (+3.9%) in the positive direction of loading. The damage photos provided in this section for all three specimens were selected from the failure direction for each specimen (positive direction for specimen 1 and negative direction for specimens 2 and 3). At +0.53% drift, several diagonal shear cracks, horizontal flexural cracks, and vertical cracks were observed at the base of specimen 1. The vertical cracks demonstrated the ineffectiveness of the tie reinforcement in this wall and they were likely also related to the use of headed bars for the vertical ties. No concrete spalling was evident in specimen 1 at the failure drift level (+1.7%), which was due to the steel angles and compression-only steel bars used to strengthen the toes of the wall.

Breakout failure of the north connector group was the ultimate failure mode of specimen 1. The headed bars were ineffective as vertical tie reinforcement, and the rectilinear tie bars 1 and 2 around the connectors were inadequate as transverse and longitudinal ties, ultimately resulting in the formation of connector breakout failure planes (Fig. 11). Upon excavation of the damaged concrete after the completion of the test, the same failure mechanism was observed at the south end connectors.

The damage to specimen 2 at the third cycle of the first displacement-controlled loading level (-0.62% drift) included shear and flexural cracks (**Fig. 12**). However, unlike specimen 1, specimen 2 did not have significant vertical cracks because the vertical headed tie bars were eliminated and the redesigned U-bar tie reinforcement was more effective. At the validation-level drift (-2.1%), extensive concrete crushing and splitting developed at the south toe of specimen 2. Concentration of cracking was also observed around the shear dowels, which extended to the south toe along the longitudinal tie bars, contributing to the concrete degradation at the toe. As the test continued, more concrete crushing at the south toe of the wall was observed, with significantly less damage at the north toe, as can be seen in Fig. 12 at the last applied drift cycle at -4.7%. Loss of concrete confinement around the connectors was the main cause of failure in specimen 2. Excavation of the damaged concrete after testing revealed

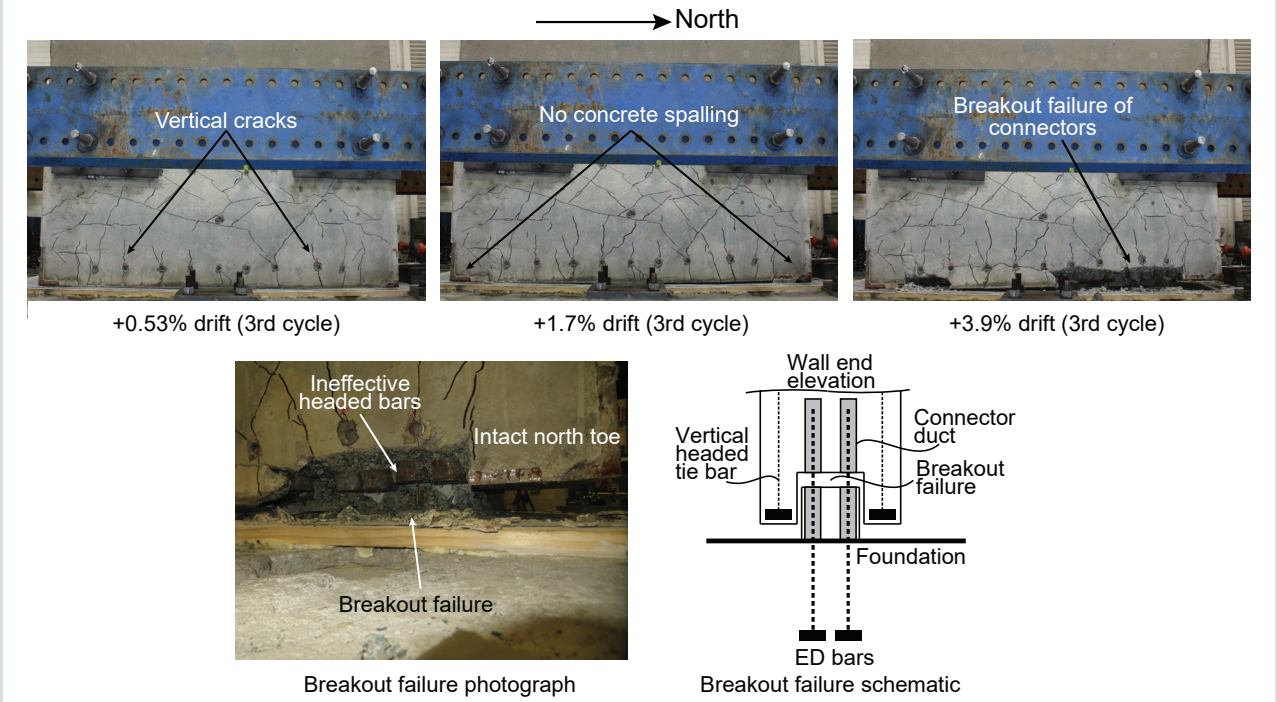

Figure 11. Damage and failure in specimen 1. Note: ED = energy-dissipation.

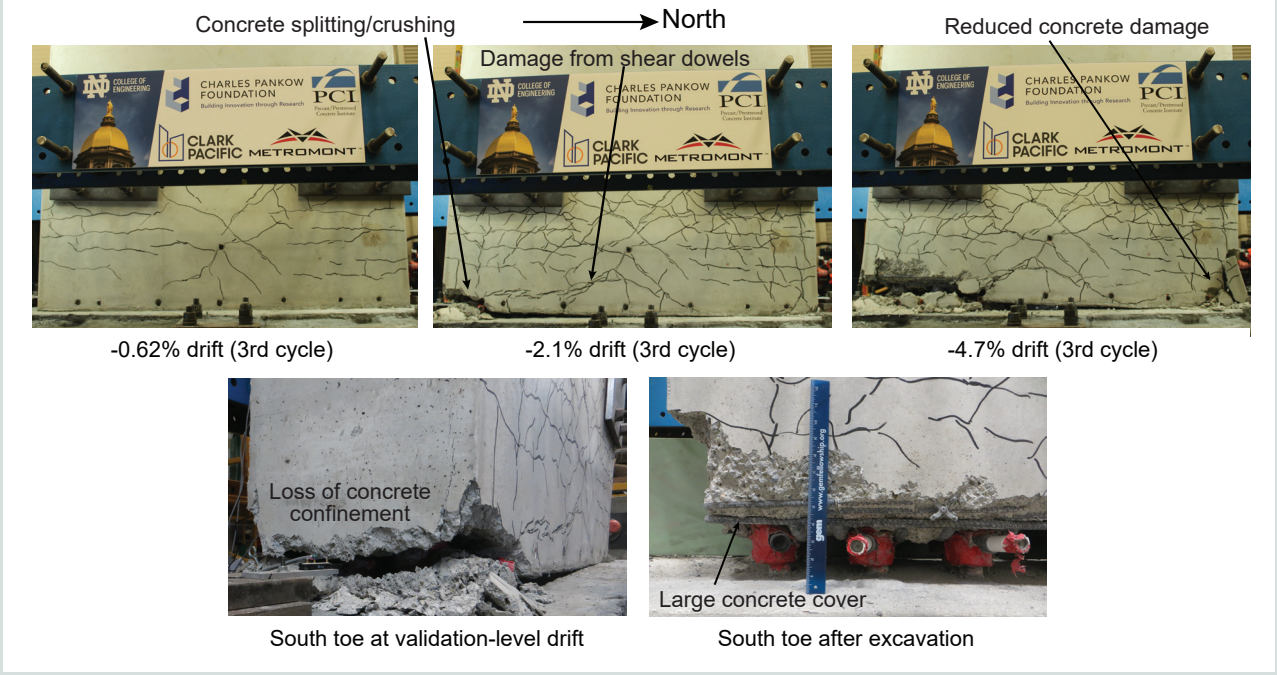

Figure 12. Damage and failure in specimen 2.

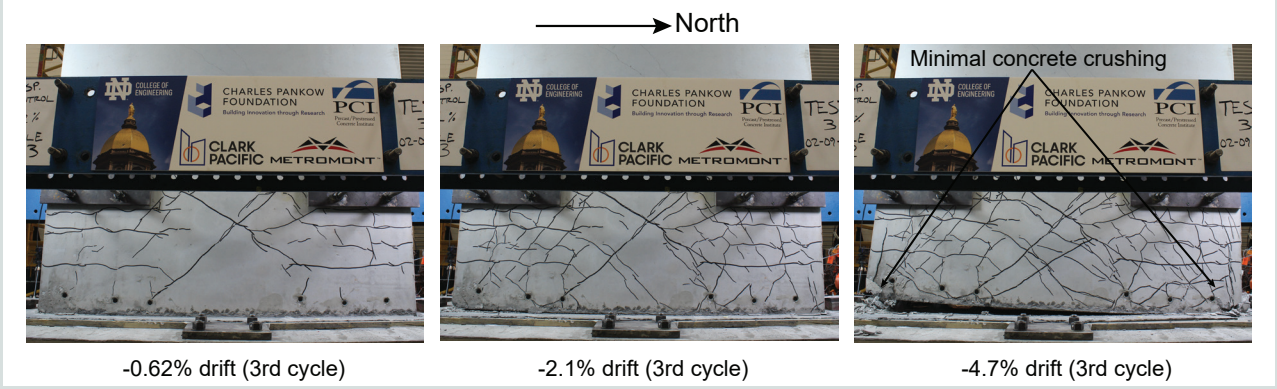

Figure 13. Damage and failure in specimen 3.

that the placement of the connector grout-in tubes below the confinement hoops and tie reinforcement (Fig. 12) resulted in excessive cover to the reinforcement at the bottom of the wall, which contributed to this failure.

Specimen 3 had significantly reduced damage throughout the test, as shown in **Fig. 13**, at the same drift levels provided for specimen 2 in Fig. 12. Concrete crushing in specimen 3 initiated late at 3.1% drift and remained limited even by the end of the test. These results demonstrate that the design and detailing modifications of specimen 3 improved the concrete behavior at the wall toes, which allowed the energy-dissipation bar connectors to function as intended by effectively transferring the connection forces through the tie reinforcement in tension and concrete struts in compression. Removal of the shear dowels in specimen 3 reduced the concentration of damage at the bottom of the wall by distributing the resistance against base sliding to the dowel action of the energy-dissipation bars. Furthermore, intentional unbonding of the energy-dissipation bars over a length of three times the energy-dissipation bar diameter ($3d_{ED}$) inside the connectors significantly improved the performance of the concrete at the wall toes by transferring the energy-dissipation bar forces further up in the wall.

Importantly, the improved behavior of specimen 3 was achieved with no increase in the overall length of the connectors since the bonded length of the energy-dissipation bars was decreased to $12d_{ED}$ to maintain the same total length of $15d_{ED}$ as the other two specimens and as recommended for no. 11 (36M) energy-dissipation bars by Aragon et al.[11] This

intentional unbonding detail is recommended for the flexural reinforcing bars in the boundary regions of special reinforced concrete shear walls, as was also experimentally demonstrated by Barbachyn et al.[19] for the boundary reinforcement of coupled reinforced concrete shear wall structures.

Reducing the clear concrete cover for the tie and confinement reinforcement to ¾ in. (19 mm) by moving the connector grout-in tubes above the bottommost hoop and tie bars improved the effectiveness of the concrete around the energy-dissipation bar connectors in specimen 3. Thus, the hoop and tie reinforcement around the connectors should be detailed with a specified clear cover not exceeding the minimum cover of ¾ in. required by ACI 318-19[2] for shear walls. The placement of the grout-in/grout-out tubes for the connector ducts should be specified by the designer so that their detailing is explicitly incorporated into the shop drawings. The connector ducts should be a few inches longer than the length of the energy-dissipation bars inside the connectors to allow for construction tolerances and also accommodate the placement of the grout-out tubes at least 1 in. (25 mm) above the end of the bar. The inner diameter of the connector duct should be selected to provide a tolerance of about ½ to 1 in. all around the energy-dissipation bar.

Figure 14 shows the top surface of each foundation after removal of the wall and base joint grout pad in specimens 2 and 3. The foundation damage in specimen 2 was limited to well-distributed cracks originating from the energy-dissipation bars. The largest marked crack was 0.03 in. (0.76 mm) wide. For specimen 3, significant splitting and crushing of the foundation concrete was observed, especially on the north side. The increased foundation damage in specimen 3 is attributed to the transfer of greater compression stresses from the wall toes and greater shear stresses from the dowel action of the energy-dissipation bars.

Reinforcing bar tension strains

Table 6 summarizes the tension strain data from the gauged energy-dissipation bars and tie bars in each test. The energy-dissipation bars in all three specimens yielded during the first displacement-controlled loading level. The maximum strains recorded by the energy-dissipation bar gauges occurred before the failure of the three specimens, indicating that higher strains likely developed in the bars but were not measured due to gauge failure.

The strain gauge data show that the vertical tie bars yielded as designed in all three specimens. The transverse ties were designed to not yield; however, the rectilinear tie bars 1 and 2 in specimen 1 yielded early in the test (in the first displacement-controlled loading level to 0.53% drift), which supports the previous statement in the progression of damage section that the provided tie reinforcement detail was inadequate. In specimens 2 and 3, the horizontal legs of the vertical U bars were designed as transverse ties and they did not yield, indicating that using U bars as vertical and transverse ties around the energy-dissipation bar connectors was effective. Thus, U bars instead of headed bars should be used as tie reinforcement. In general, smaller-diameter U bars are recommended to minimize the bend radius of the bars for better detailing and placement of the reinforcement in the connection region.

Although the longitudinal tie bars did not yield in specimen 1, details of the longitudinal reinforcement at the bottom of the wall were changed in specimen 2 to improve the effectiveness of the longitudinal ties and to reduce congestion at the bottom of the wall. Similarly, even though the longitudinal tie bars in specimen 2 did not yield, the design was further modified in specimen 3 by adding the area of the bottommost shear bars to the longitudinal tie reinforcement area. This change was made because the longitudinal tie bars in specimen 2 had a considerably larger diameter (no. 8 [25M]) than the shear bars (no. 4 [13M]). As these different size bars were placed adjacent to each other, it is likely that the longitudinal tie bars with the much greater axial stiffness also contributed to the shear resistance of the wall. To avoid this condition and also minimize congestion, it is recommended that the first shear reinforcement bar at the bottom of the wall be removed and its area be added to the longitudinal tie reinforcement area.

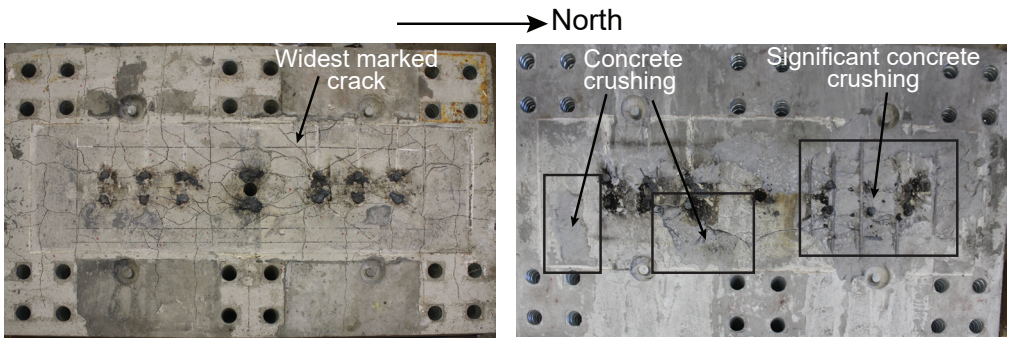

Figure 14. Foundation damage.

Table 6. Reinforcing bar tension strain data

			Specimen 1	Specimen 2	Specimen 3	
Energy-dissipation bar	Drift at yield, %	(+)	0.53	0.62	0.62	
		(-)	0.53	0.62	0.62	
	Maximum recorded strain	(+)	$3.8\varepsilon_{y,ED}$	$3.3\varepsilon_{y,ED}$	$4.5\varepsilon_{y,ED}$	
		(-)	$2.3\varepsilon_{y,ED}$	$2.9\varepsilon_{y,ED}$	$2.9\varepsilon_{y,ED}$	
	Drift at maximum recorded strain, %	(+)	1.2	0.90	1.4	
		(-)	0.79	0.90	0.90	
Vertical tie bar	Drift at yield, %	(+)	0.53	0.90	2.1	
		(-)	n.d.	n.d.	2.1	
	Maximum recorded strain	(+)	$1.5\varepsilon_{y,vt}$	$4.5\varepsilon_{y,vt}$	$2.2\varepsilon_{y,vt}$	
		(-)	n.d.	n.d.	$3.5\varepsilon_{y,vt}$	
	Drift at maximum recorded strain, %	(+)	1.7	2.1	2.1	
		(-)	n.d.	n.d.	2.1	
Transverse tie bar	Drift at yield, %	(+)	0.53	no yield	no yield	
		(-)	n.d.	no yield	no yield	
	Maximum recorded strain	(+)	$3.5\varepsilon_{y,tt}$	$0.65\varepsilon_{y,tt}$	$0.65\varepsilon_{y,tt}$	
		(-)	n.d.	$0.66\varepsilon_{y,tt}$	$0.26\varepsilon_{y,tt}$	
	Drift at maximum recorded strain, %	(+)	0.79	3.1	3.1	
		(-)	n.d.	2.1	1.4	
Longitudinal tie bar					Layer 1	Layer 2
	Drift at yield, %	(+)	no yield	no yield	4.7	no yield
		(-)	n.d.	no yield	3.1	1.4
	Maximum recorded strain	(+)	$0.53\varepsilon_{y,lt}$	$0.75\varepsilon_{y,lt}$	$1.5\varepsilon_{y,lt}$	$0.75\varepsilon_{y,lt}$
		(-)	n.d.	$0.75\varepsilon_{y,lt}$	$1.5\varepsilon_{y,lt}$	$1.3\varepsilon_{y,lt}$
	Drift at maximum recorded strain, %	(+)	1.2	4.7	4.7	4.7
		(-)	n.d.	2.1	3.1	2.1

Note: n.d. = no data; $\varepsilon_{y,ED}$ = yield strain of energy-dissipation bar; $\varepsilon_{y,lt}$ = yield strain of longitudinal tie bar; $\varepsilon_{y,tt}$ = yield strain of transverse tie bar; $\varepsilon_{y,vt}$, = yield strain of vertical tie bar.

The revised design in specimen 3 included two layers of no. 7 (22M) longitudinal bars to serve as both longitudinal tie reinforcement and bottommost shear reinforcement. During the testing of specimen 3, both of these longitudinal bar layers yielded, with the top layer yielding at an earlier drift of 1.4% before the validation-level drift. This outcome may have occurred because intentional unbonding of the energy-dissipation bars transferred forces higher up in the wall, resulting in higher demands on the top layer. Since the longitudinal tie reinforcement was designed to not yield, the strut-and-tie design of the connectors may need to be revised in future research. The large tension strains measured in the longitudinal bars demonstrate the importance of anchoring these bars inside the boundary region at each end of the wall to develop the yield strength of the steel.

Components of deformation

The contributions of base rotation, base sliding, shear (diagonal tension/compression deformation over the wall weight), and flexure (over the wall height) to the total wall lateral drift were computed at the positive and negative peak drifts during the first cycle of each displacement-controlled load level. The calculation of shear deformations over the wall height used diagonal string potentiometers based on the method outlined by Oesterle et al.[20] Once the contributions of base sliding,

shear over the wall height, and base rotation were calculated, the remaining portion of the total wall drift was attributed to flexural deformations over the wall height. In specimen 1, the diagonal string potentiometers used to record the shear deformations did not provide reliable data. Therefore, after calculating the contributions of base sliding and base rotation, the remaining portion of drift was attributed to combined shear and flexural deformations over the wall height. For specimens 1 and 2, the displacement transducers used to measure the deformation components were removed from the wall during the last displacement-controlled loading level to protect the sensors from spalling concrete. Therefore, the deformation components of these two specimens were calculated up to (but not including) the last loading level.

The contribution of base sliding in specimens 1 and 2 did not exceed 10% of the total wall drift due to the use of shear dowels in these specimens (**Fig. 15**). In specimen 3, the contribution of base sliding at the validation-level drift of 2.1% reached about 12% in the positive direction and 16% in the negative direction. The corresponding base sliding displacements were about 0.33 in. (8.4 mm) and 0.44 in. (11.2 mm), respectively, and exceeded the 0.06 in. (1.5 mm) limit specified by ACI 550.6-19[7] for base sliding. Although the amount of base sliding exceeded the ACI 550.6-19 limit, this sliding did not cause failure. This finding suggests that the base sliding limit specified by ACI 550.6-19, which is set for post-tensioned precast concrete shear walls, is not applicable to precast concrete shear walls without post-tensioning steel. Base sliding in post-tensioned walls is typically smaller due to the additional compression transferred at the wall-to-foundation joint interface.[3–5]

The total flexural deformation, including base rotation and flexural deformations over the wall height, was the dominant type of deformation in all three specimens. Base rotation is a desired mode of deformation because it is associated with energy dissipation through yielding of the flexural bars. This

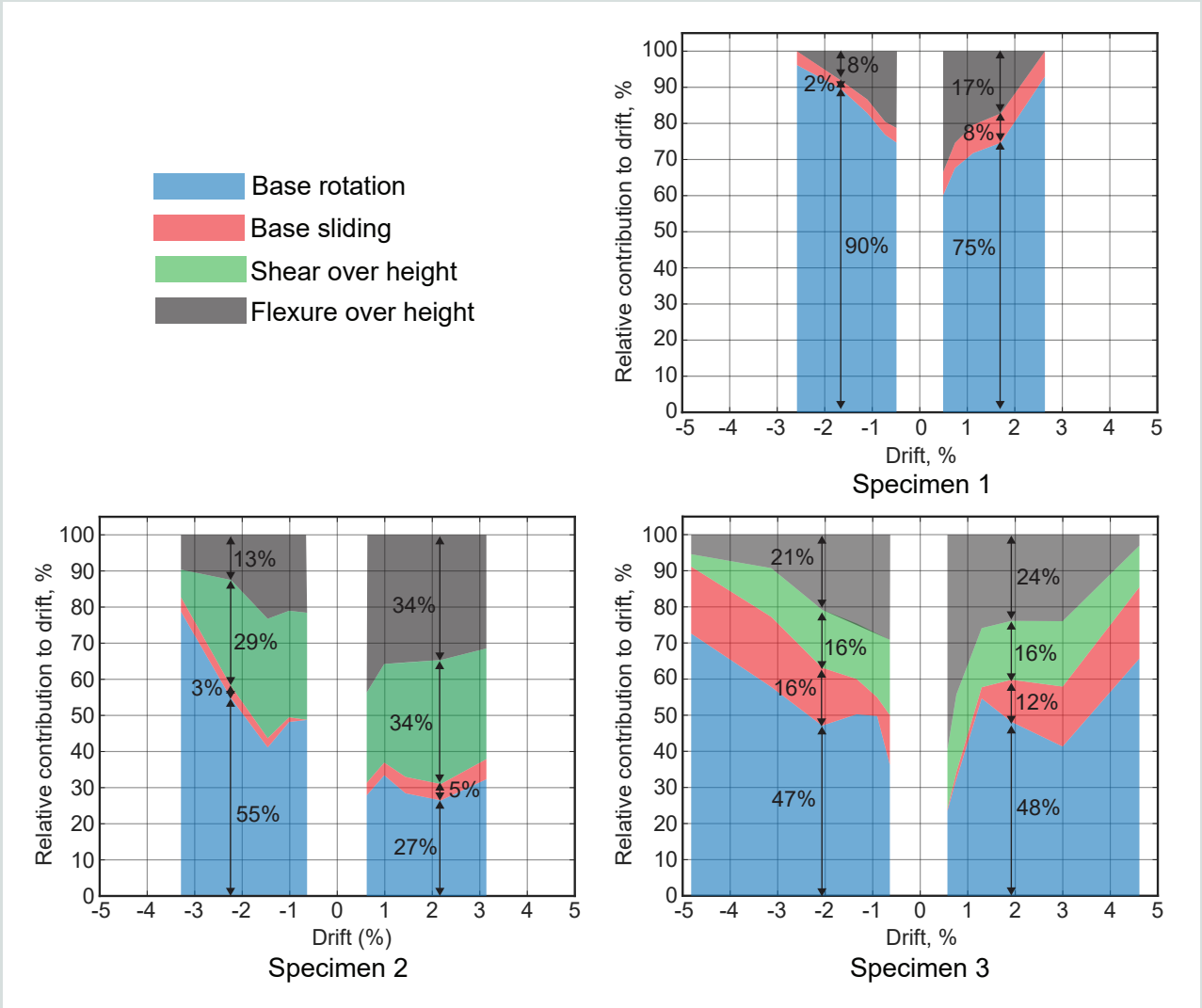

Figure 15. Components of deformation.

deformation component was the highest contributor to the total drift of the three specimens throughout the displacement-controlled loading series. The base rotation of specimen 1 was significantly greater than that in specimens 2 and 3. This was likely because of the welded compression-only vertical bars at the toes of specimen 1, which reduced the flexural deformations over the wall height.

The total shear deformation, which includes base sliding and shear (diagonal tension/compression) deformations over the wall height, was a smaller but not negligible component of total drift, as may be expected for shear walls with a base moment–to–shear ratio of two times the length of the wall ($M_b/V_b = 2.0\ell_w$). The average contribution of the total shear deformation in the positive and negative directions of loading at the validation-level drift (2.1%) was 36% for specimen 2 and 30% for specimen 3.

Comparing the relative deformation components for specimens 2 and 3, removal of the shear dowels in specimen 3 did not affect the total shear or flexural deformations. Instead, specimen 3 had increased base sliding but smaller diagonal-tension/compression deformations over the wall height, adding up to similar amounts of total shear deformation in the two walls. Specifically, the average (considering positive and negative loading directions) contributions of base sliding and shear (diagonal-tension/compression) deformations over the wall height at the validation-level drift were 4% and 32%, respectively, in specimen 2, and 14% and 16%, respectively, in specimen 3.

Secant lateral stiffness and relative energy dissipation

Table 7 provides the secant lateral stiffness between drift angles of 1/10 and -1/10 of the maximum applied drift during the failure drift cycle (1.7%) for specimen 1 and during the third validation-level drift cycle (2.1%) for specimens 2 and 3. The secant stiffness is provided as a proportion of the initial lateral stiffness K_i, which was calculated per ACI 550.6-19[7] as the slope of the line connecting the origin to 0.75 times the nominal strength V_n of the wall (calculated using the measured compression strength of unconfined concrete and measured yield strength of the energy-dissipation bars). ACI 550.6-19 requires the secant stiffness to be 0.1 times the initial stiffness or greater, because if the stiffness degradation of the wall is large (that is, the secant stiffness in proportion to the initial stiffness is low), large displacements will result from small changes in lateral load during an earthquake. Similar to the base sliding limit discussed in the previous section, the secant stiffness limit specified by ACI 550.6-19 is not applicable to precast concrete shear walls without post-tensioning steel. Nonetheless, both specimens 2 and 3 satisfied this requirement, whereas specimen 1 had a larger amount of stiffness degradation in the negative loading direction than the ACI 550.6-19 limit. In all three specimens, the stiffness degradation in the negative direction was more than that in the positive direction. For specimens 2 and 3, this finding is likely related to the failure of the wall in the negative loading direction, whereas for specimen 1, it may be related to the higher initial stiffness of the wall in the negative direction.

Figure 16 shows the energy-dissipation ratios calculated for the third cycle at each drift level of the displacement-controlled loading series based on the method described in ACI 550.6-19. The relative energy-dissipation ratio is required by ACI 550.6-19 to be at least 0.125 at the validation-level drift. The relative energy-dissipation ratios for all three specimens were similar and well above this minimum requirement.

Neutral axis location at wall base

The neutral axis location measuring the contact (compression) length at the base of each wall specimen was calculated using the data from the linear variable displacement transducers across the wall-to-foundation joint interface. **Figure 17** shows the compression length (normalized with respect to the wall length) calculated for the first cycle of each load and drift level from the testing of the three specimens.

All three specimens experienced a rapid reduction in the compression length early in each test, which was related to the initiation of gap opening at the wall-to-foundation joint interface. The subsequent changes in compression length followed similar trends in the failure (negative) loading direction for specimens 2 and 3. Specifically, both specimens experienced a gradual reduction in compression length, followed by a sudden growth at the failure drift (2.1% for specimen 2 and 3.1% for specimen 3), followed by further reduction of the compression length at the subsequent drift level. The growth in the compression length at the failure drift is indicative of compression stress loss due to crushing of concrete at the

Table 7. Secant lateral stiffness

Specimen	Drift level, %		Initial stiffness K_i, kip/in.		Secant stiffness	
	(+)	(-)	(+)	(-)	(+)	(-)
1	1.7	1.7	433	520	$0.14K_i$	$0.08K_i$
2	2.1	2.1	291	309	$0.26K_i$	$0.16K_i$
3	2.1	2.1	318	326	$0.22K_i$	$0.17K_i$

Note: 1 kip/in. = 175.1 kN/m.

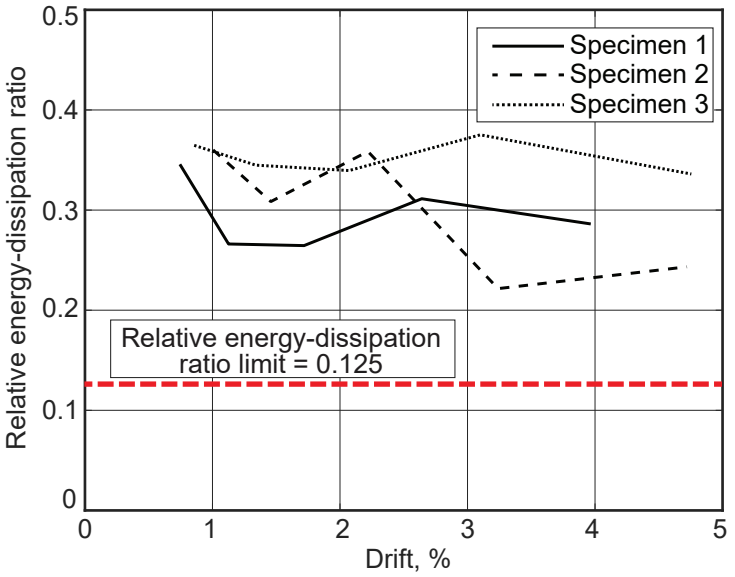

Figure 16. Relative energy-dissipation ratio.

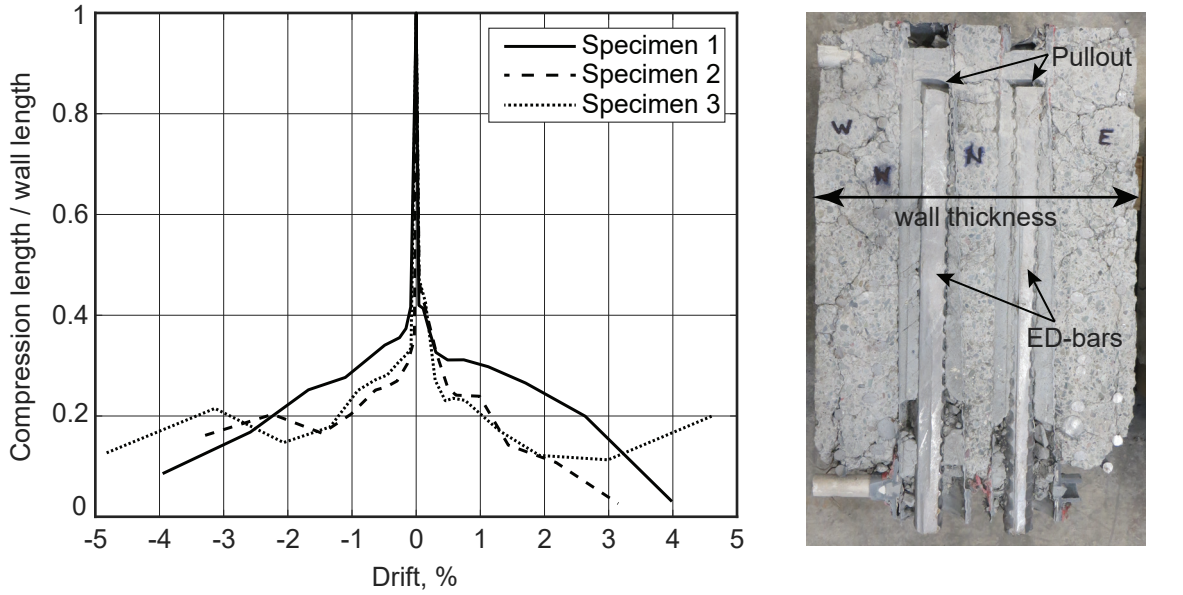

Figure 17. Failure modes of test specimens. Note: ED = energy-dissipation.

boundary region of the wall. This is because a larger area of concrete needs to be in compression to satisfy axial equilibrium while the concrete compression strength is lost due to crushing. In contrast, the decrease in compression length during the subsequent drift level of each wall is indicative of tension stress loss in the energy-dissipation bars due to pullout of the bars from the connectors. This is because as the tension forces in the bars decrease, a shorter concrete compression length is needed to provide adequate compression forces to achieve axial equilibrium.

Based on these changes in compression length with increased drift, as well as the aforementioned observations for the damage progression of each wall, this study concludes that the failure of specimens 2 and 3 occurred due to the crushing of the concrete in compression. Crushing of concrete also result-

ed in the loss of confinement around the connectors, which led to in further loss of lateral load in the subsequent drift cycle for each wall due to pullout of the energy-dissipation bars in tension. To assess this conclusion, a section-cut was taken through the outermost northern layer of connectors across the wall thickness in specimen 2. As shown in Fig. 17, a gap was observed between the end of the energy-dissipation bars and the grout in both connectors, providing physical evidence that the energy-dissipation bars had pulled out. Despite the fact that specimens 2 and 3 had the same failure mechanism, crushing of the concrete occurred at a significantly greater drift level in specimen 3 than in specimen 2 (3.1% versus 2.1%). Concrete crushing and ultimate failure in the positive loading direction of specimen 3 were further delayed up to a drift level of 4.7%, consistent with the elongation of compression length at this drift level as shown in Fig. 17. Based on this significantly improved behavior, the design and details in specimen 3 are recommended for the use of the proposed connectors in practice.

In comparison with specimens 2 and 3, the trends in Fig. 17 show that specimen 1 had a consistent shortening of compression length throughout the test. The lack of elongation in the compression length of specimen 1 was because the use of steel angles and compression-only bars at the toes prevented compression failure of this wall. Instead, breakout failure of the energy-dissipation bar connectors in tension was the predominant failure mode, as discussed earlier in the lateral load-drift behavior and progression of damage sections of this article. In addition to the greater energy-dissipation bar area, the smaller compression length of specimen 1 likely contributed to the greater peak lateral strength achieved by this wall as compared with the peak strengths of specimens 2 and 3.

Conclusion

In this study, three precast concrete shear walls were designed, constructed, and tested to evaluate the use of nonproprietary, short-grouted corrugated steel straight ducts to connect ductile energy-dissipating reinforcing bars crossing horizontal joints. In this type of connection, the energy-dissipation bars are terminated inside the connectors, and the bar forces are transferred into the wall through the design of vertical, transverse, and longitudinal tie reinforcing bars around the connectors. The performance of the three specimens was evaluated according to the seismic acceptance criteria for special precast concrete shear walls in ACI 550.6-19.[7] Based on the results from this study, the following conclusions were made:

- The precast concrete shear wall specimens tested with the proposed connectors had better performance when compared with previously tested precast concrete shear walls with Type II grouted mechanical splices.

- Two of the tested walls (specimens 2 and 3) satisfied the minimum energy-dissipation and maximum stiffness-degradation requirements of ACI 550.6-19. However, only one wall (specimen 3) also satisfied the lateral strength loss limit (maximum loss of 20% from the peak lateral strength in each direction of loading) at the validation-level drift.

- The performance of specimen 3 demonstrates that nonproprietary short-grouted connectors using materials readily available in the construction industry can achieve ductile behavior of special precast concrete shear walls for use in high-seismic regions.

- Specimen 1, which used headed bars for the vertical tie reinforcement, failed due to breakout of the connector group at each end of the wall. The headed bars were ineffective in transferring the energy-dissipation bar forces across the wall thickness.

- The use of U bars as the vertical and transverse tie reinforcement around the connectors in specimens 2 and 3 significantly improved the performance of these walls. Thus, U bars instead of headed bars should be used as tie reinforcement. Smaller diameter U bars should be preferred to minimize the bend radius of the bars for better detailing and placement of the reinforcement in the connection region.

- Failure in both specimens 2 and 3 initiated due to compression failure of concrete around the connectors. Loss of confinement from the surrounding concrete subsequently resulted in tension failure (pullout) of the energy-dissipation bars from the connectors.

- In specimen 3, intentional unbonding of the energy-dissipation bars over a length of three times the energy-dissipation bar diameter ($3d_{ED}$) inside the connectors significantly improved the performance of the concrete at the wall toes by transferring the energy-dissipation bar forces further up in the wall. This improved behavior was achieved with no increase in the overall length of the connectors since the bonded length of the energy-dissipation bars was decreased to $12d_{ED}$ to maintain the same total length ($15d_{ED}$) as the other two specimens and as recommended for no. 11 (36M) energy-dissipation bars by Aragon et al.[11] This intentional unbonding detail is recommended for flexural reinforcing bars in the boundary regions of special reinforced concrete shear walls in practice.

- The hoop and tie reinforcement around the connectors should be detailed with a specified clear cover not exceeding the minimum cover required by ACI 318-19[2] for shear walls.

- The connector duct should be a few inches longer than the length of the energy-dissipation bar inside the connector to allow for construction tolerances and accommodate the placement of the grout-out tube at least 1 in. (25 mm) above the end of the bar. The inner diameter of the connector duct should be selected to provide a tolerance of about ½ to 1 in. (13 to 25 mm) all around the energy-dissipation bar.

- The placement of the grout-in/grout-out tubes for the connector ducts should be specified so that their detailing is explicitly incorporated into the shop drawings.

- Even though specimen 3 satisfied the validation-level drift requirement of ACI 550.6-19, the longitudinal tie reinforcement in this wall yielded before the validation-level drift. Since this reinforcement was designed not to yield, the strut-and-tie design of the connectors may need to be revised in future research.

- The longitudinal tie reinforcing bars should be anchored inside the boundary region at each end of the wall to develop the yield strength of the steel.

- To ensure effective shear and connector design and minimize congestion at the base of the wall, the bottom-most shear reinforcing bar should be removed and its area should be added to the connector longitudinal tie reinforcement area.

- The base rotation, which is the most desirable mode of deformation, was the largest contributor to the total drift of the wall specimens.

- The total shear deformation, which includes base sliding and diagonal tension/compression deformations over the wall height, was a smaller but not negligible component of about 30% to 36% of the total wall drift. This amount of shear deformation may be expected for shear walls with a base moment–to–shear ratio of two times the length of the wall.

- In specimen 3, the contribution of base sliding at the validation-level drift reached about 12% to 16% of the total wall drift. The corresponding base sliding displacements were about 0.33 to 0.44 in. (8.4 to 11.2 mm), and exceeded the 0.06 in. (1.5 mm) limit specified by ACI 550.6-19 for base sliding. Although the amount of base sliding exceeded the limit, it did not cause the failure of specimen 3. This finding suggests that the maximum base sliding limit specified by ACI 550.6-19 for post-tensioned precast concrete shear walls is not applicable to precast concrete shear walls without post-tensioning steel.

Acknowledgments

This research was conducted with funding from the Charles Pankow Foundation, the Precast/Prestressed Concrete Institute (PCI), Clark Pacific, and Metromont Corporation, and the test specimens were donated by Clark Pacific and Metromont Corporation. This support is gratefully acknowledged. The authors thank the PCI Research and Development Council, the PCI Central Region, as well as members of the Industry Advisory Committee, including Suzanne Aultman of Metromont Corporation; Keith Bauer of Buehler Engineering; Kal Benuska of John A. Martin & Associates; Jared Brewe of PCI; Harry Gleich of Gleich Engineering and Associates LLC; Les Kempers of GPRM Prestress; Kevin Kirkley of Tindall Corporation; Walter Korkosz of Consulting Engineers Group; Donald Meinheit of Wiss, Janney, Elstner Associates; Andrew Osborn of Wiss, Janney, Elstner Associates; and Wael Zatar of Marshall University. Salah Khalaf of Clark Pacific and Fanfu Fan of Metromont Corporation facilitated the construction of the test specimens, Christian Dennis (former graduate student at the University of Notre Dame) assisted with the laboratory testing of specimen 1, and Dr. Brad Weldon (University of Notre Dame) assisted with specimen erection. The authors also thank StresCore Inc. for assisting in the handling and disposal of the test specimens. Any opinions, findings, conclusions, and recommendations expressed in this article are those of the authors and do not necessarily reflect the views of the individuals and organizations acknowledged.

References

1. ACI (American Concrete Institute). 2019. *Requirements for Design of a Special Unbonded Post-Tensioned Precast Shear Wall Satisfying ACI 550.6 (ACI 550.7) and Commentary*. Farmington Hills, MI: ACI.

2. ACI. 2019. *Building Code Requirements for Structural Concrete (ACI 318-19) and Commentary (ACI 318R-19)*. Farmington Hills, MI: ACI.

3. Smith, B. J., Y. C. Kurama, and M. J. McGinnis. 2011. "Design and Measured Behavior of a Hybrid Precast Concrete Wall Specimen for Seismic Regions." *Journal of Structural Engineering* 137 (10): 1052–1062. https://doi.org/10.1061/(ASCE)ST.1943-541X.0000327.

4. Smith, B. J., Y. C. Kurama, and M. J. McGinnis. 2013. "Behavior of Precast Concrete Shear Walls for Seismic Regions: Comparison of Hybrid and Emulative Specimens." *Journal of Structural Engineering* 139 (11): 1917–1927. https://doi.org/10.1061/(ASCE)ST.1943-541X.0000755.

5. Smith, B. J., Y. C. Kurama, and M. J. McGinnis. 2015. "Perforated Hybrid Precast Shear Walls for Seismic Regions." *ACI Structural Journal* 112 (3): 359–370. https://doi.org/10.14359/51687410.

6. ASTM International. 2016. *Standard Specification for Deformed and Plain Low-Alloy Steel Bars for Concrete Reinforcement*. ASTM A706/A706M-16. West Conshohocken, PA: ASTM International.

7. ACI. 2019. *Acceptance Criteria for Special Unbonded Post-Tensioned Precast Structural Walls Based on Validation Testing and Commentary*. ACI 550.6-19. Farmington Hills, MI: ACI.

8. ICC-ES (ICC Evaluation Service). 2015. *Acceptance Criteria for Mechanical Connector Systems for Steel Reinforcing Bars*. AC133. Whittier, CA: ICC-ES.

9. Aragon, T. A., Y. C. Kurama, and D. F. Meinheit. 2017. "A Type III Grouted Seismic Connector for Precast Concrete Structures." *PCI Journal* 62 (5): 75–88. https://doi.org/10.15554/pcij62.5-05.

10. Aragon, T. A., Y. C. Kurama, and D. F. Meinheit. 2019. "Effects of Grout and Energy Dissipating Bar Properties on a Type III Grouted Seismic Connection for Precast Structures." *PCI Journal* 64 (1): 31–48. https://doi.org/10.15554/pcij64.1-03.

11. Aragon, T. A., Y. C. Kurama, and D. F. Meinheit. 2020. "Behavior of Ductile Short-Grouted Seismic Reinforcing Bar-to-Foundation Connections Under Adverse Construction Conditions." *PCI Journal* 65 (4): 33–50. https://doi.org/10.15554/pcij65.4-01.

12. PCI Handbook Committee. 2017. *PCI Design Handbook*. MNL 120-17. Chicago, IL: PCI. https://doi.org/10.15554/MNL-120-17.

13. ASTM International. 2022. *Standard Test Methods and Definitions for Mechanical Testing of Steel Products*. ASTM A370-22. West Conshohocken, PA: ASTM International.

14. ASTM International. 2022. *Standard Test Method for Static Modulus of Elasticity and Poisson's Ratio of Concrete in Compression*. ASTM C469-22. West Conshohocken, PA: ASTM International.

15. ASTM International. 2021. *Standard Test Method for Compressive Strength of Cylindrical Concrete Specimens*. ASTM C39/C39M-21. West Conshohocken, PA: ASTM International.

16. ASTM International. 2017 *Standard Test Method for Splitting Tensile Strength of Cylindrical Concrete Specimens*. ASTM C496-17. West Conshohocken, PA: ASTM International.

17. ASTM International. 2016. *Standard Test Method for Flexural Strength of Concrete (Using Simple Beam with Center-Point Loading).* ASTM C293/C293M-16. West Conshohocken, PA: ASTM International.

18. ASTM International. 2020. *Standard Test Method for Compressive Strength of Hydraulic Cement Mortars (Using 2-in. or [50 mm] Cube Specimens)*. ASTM C109/C109M-20. West Conshohocken, PA: ASTM International.

19. Barbachyn, S. M., Y. C. Kurama, M. J. McGinnis, and R. Sause. 2016. "Coupled Shear Wall with Fully Post-Tensioned Beams and Unbonded Rebar at Toes." *ACI Structural Journal* 113 (6): 1381–1392. https://doi.org/10.14359/51689252.

20. Oesterle, R. G., A. E. Fiorato, L. S. Johal, J. E. Carpenter, H. G. Russell, and W. G. Corley. 1976. *Earthquake Resistant Structural Walls—Tests of Isolated Walls*. National Science Foundation report NSF/RA-76081S. Skokie, IL: Portland Cement Association. https://nehrpsearch.nist.gov/article/PB-271%20467/3/XAB.

Notation

A_{ED} = total area of energy-dissipation bar or bars in one layer across wall thickness

A_g = gross area of wall cross section

$A_{\ell t}$ = total required area of longitudinal tie reinforcement to transfer tension force in AED

A_{tt} = total required area of transverse tie reinforcement to transfer tension force in AED

A_{vt} = total required area of vertical tie reinforcement to transfer tension force in AED

d_{ED} = diameter of energy-dissipation bar

E_c = modulus of elasticity of concrete

E_{cg} = modulus of elasticity of grout

$E_{cg,td}$ = modulus of elasticity of grout at wall test day

$E_{c,td}$ = modulus of elasticity of concrete at wall test day

E_s = modulus of elasticity of reinforcing bar

f'_c = specified compression strength of concrete

$f'_{c,28d}$ = compression strength of concrete at 28 days

f'_{cg} = compression strength of grout

$f'_{cg,28d}$ = compression strength of grout at 28 days

$f'_{cg,td}$ = compression strength of grout at wall test day

$f'_{c,td}$ = compression strength of concrete at wall test day

$f_{r,28d}$ = modulus of rupture of concrete at 28 days

$f_{r,td}$ = modulus of rupture of concrete at wall test day

f_t = split cylinder tension strength of concrete

$f_{t,28d}$ = split cylinder tension strength of concrete at 28 days

f_{tg} = split cylinder tension strength of grout

$f_{tg,28d}$ = split cylinder tension strength of grout at 28 days

$f_{tg,td}$ = split cylinder tension strength of grout at wall test day

$f_{t,td}$ = split cylinder tension strength of concrete at wall test day

f_u = ultimate (peak) strength of reinforcing bar

$f_{u,c}$ = ultimate (peak) strength of confinement hoop bar

$f_{u,ED}$ = ultimate (peak) strength of energy-dissipation bar

$f_{u,\ell t}$ = ultimate (peak) strength of longitudinal tie bar

$f_{u,tt}$ = ultimate (peak) strength of transverse tie bar

$f_{u,,vt}$ = ultimate (peak) strength of vertical tie bar

f_y = yield strength of reinforcing bar

$f_{y,c}$ = yield strength of confinement hoop bar

$f_{y,ED}$ = yield strength of energy-dissipation bar

$f_{y,\ell t}$ = yield strength of longitudinal tie bar

$f_{y,tt}$ = yield strength of transverse tie bar

$f_{y,vt}$ = yield strength of vertical tie bar

K_i = initial lateral stiffness of wall specimen

ℓ_b = bonded length of energy-dissipation bar

ℓ_w = length of wall specimen

M_b = base moment of wall specimen

P = total axial load at base of wall specimen

T_{ED} = total tension force in energy-dissipation bar or bars placed in one layer across wall thickness

$T_{\ell t}$ = total tension force in longitudinal tie reinforcement designed to transfer T_{ED} to wall

T_{tt} = total tension force in transverse tie reinforcement designed to tansfer T_{ED} to wall

T_{vt} = total tension force in vertical tie reinforcement designed to transfer T_{ED} to wall

V_b = base shear of wall specimen

V_{max} = measured peak (maximum) lateral (base shear) strength of wall specimen

V_n = nominal lateral (base shear) strength of wall specimen calculated using measured compression strength of unconfined concrete and measured yield strength of energy-dissipation bars

V_{pr} = probable lateral (base shear) strength of wall specimen calculated using measured compression strength of unconfined concrete and measured nonlinear stress-strain relationship of energy-dissipation bars

w/g = ratio of water weight to grout weight

$\beta_{\ell t}$ = angle of horizontal plane in strut-and-tie model (complementary to $\beta_{\ell t}$)

β_{tt} = angle of horizontal plane in strut-and-tie model (complementary to $\beta_{\ell t}$)

Δ_f = failure drift of wall specimen

ε_{fr} = strain of reinforcing bar at fracture

$\varepsilon_{fr,c}$ = strain of confinement hoop bar at fracture

$\varepsilon_{fr,ED}$ = strain of energy-dissipation bar at fracture

$\varepsilon_{fr,\ell t}$ = strain of longitudinal tie bar at fracture

$\varepsilon_{fr,tt}$ = strain of transverse tie bar at fracture

$\varepsilon_{fr,vt}$ = strain of vertical tie bar at fracture

ε_u = strain of reinforcing bar at f_u

$\varepsilon_{u,c}$ = strain of confinement hoop bar at $f_{u,c}$

$\varepsilon_{u,ED}$ = strain of energy-dissipation bar at $f_{u,ED}$

$\varepsilon_{u,\ell t}$ = strain of longitudinal tie bar at $f_{u,\ell t}$

$\varepsilon_{u,tt}$ = strain of transverse tie bar at $f_{u,tt}$

$\varepsilon_{u,vt}$ = strain of vertical tie bar at $f_{u,vt}$

ε_y = yield strain of reinforcing bar

$\varepsilon_{y,c}$ = yield strain of confinement hoop bar

$\varepsilon_{y,ED}$ = yield strain of energy-dissipation bar

$\varepsilon_{y,\ell t}$ = yield strain of longitudinal tie bar

$\varepsilon_{y,tt}$ = yield strain of transverse tie bar

$\varepsilon_{y,vt}$ = yield strain of vertical tie bar

θ = angle of vertical plane in strut-and-tie model

About the authors

Baha'a Al-Khateeb is a PhD candidate in the Department of Civil and Environmental Engineering and Earth Sciences at the University of Notre Dame in Notre Dame, Ind.

Christopher Garcia is a former MS student in the Department of Civil and Environmental Engineering and Earth Sciences at the University of Notre Dame.

Mark P. Manning, PhD, is a former research scientist in the Department of Civil and Environmental Engineering and Earth Sciences at the University of Notre Dame.

Jon Mohle, SE, is a senior product and market manager at Clark Pacific in Sacramento, Calif.

Yahya C. Kurama, PhD, PE, is a professor in the Department of Civil and Environmental Engineering and Earth Sciences at the University of Notre Dame in Notre Dame, Ind.

Abstract

This article presents results from the experimental testing of three precast concrete shear wall specimens that used nonproprietary, short-grouted corrugated steel straight duct connections for ductile energy-dissipating reinforcing bars crossing horizontal joints. In this type of connection, the energy-dissipation bars are terminated inside the connectors, and the bar forces are transferred into the precast concrete components through the design of vertical, transverse, and longitudinal tie reinforcing bars around the connectors. The performance of the specimens was evaluated against the seismic acceptance criteria for special precast concrete shear walls in the American Concrete Institute's *Acceptance Criteria for Special Unbonded Post-Tensioned Precast Structural Walls Based on Validation Testing and Commentary* (ACI 550.6-19). All three specimens outperformed a previously tested precast concrete wall with Type II grouted mechanical reinforcing bar splices in terms of drift capacity and energy dissipation. However, only one wall (specimen 3) satisfied the maximum lateral strength loss limit (20%) at the validation-level drift specified by ACI 550.6-19. Important connector design and detailing recommendations are made based on the performance differences among the specimens. These details include the bonded and intentionally unbonded lengths of the energy-dissipation bars inside the connectors, as well as design of the vertical, transverse, and longitudinal tie reinforcement around the connectors. The results demonstrate that nonproprietary short-grouted connectors using materials readily available in the construction industry can achieve ductile behavior of special precast concrete shear walls for use in high-seismic regions.

Keywords

Concrete crushing; energy-dissipation bars; grouted mechanical connectors; reinforcing bar pullout; seismic reinforced concrete testing; special shear walls; strut-and-tie design model; Type II mechanical splices.

Review policy

This paper was reviewed in accordance with the Precast/Prestressed Concrete Institute's peer-review process. The Precast/Prestressed Concrete Institute is not responsible for statements made by authors of papers in *PCI Journal*. No payment is offered.

Publishing details

This paper appears in *PCI Journal* (ISSN 0887-9672) V. 70, No. 1, January–February 2025, and can be found at https://doi.org/10.15554/pcij70.1-02. *PCI Journal* is published bimonthly by the Precast/Prestressed Concrete Institute, 8770 W. Bryn Mawr Ave., Suite 1150, Chicago, IL 60631.

Reader comments

Please address any reader comments to *PCI Journal* editor-in-chief Tom Klemens at tklemens@pci.org or Precast/Prestressed Concrete Institute, c/o *PCI Journal*, 8770 W. Bryn Mawr Ave., Suite 1150, Chicago, IL 60631.